

Alginate-derived microneedle devices for transdermal delivery of rivastigmine - application in skin mimetic model

Tânia Marisa Teixeira Guimarães

Dissertation for the Degree of Master in Science in Bioengineering at the Faculdade de Engenharia and Instituto Ciências Biomédicas Abel Salazar da Universidade do Porto

Supervisor: Doutora Tânia Moniz

Co-supervisor: Doutora Sofia Lima

September 2021

“Everything is theoretically impossible until it is done”
Robert A. Heinlein

Acknowledgments

Symbolically I would like to thank all the people who made this project possible, directly and indirectly.

First of all, to Professor Maria Rangel for suggesting me this research group. Without her, I wouldn't have met all these amazing people.

I would like to leave a big thank you to professor Salette Reis for allowing me to be part of her group. She was willing to accept me with open arms for an innovative project full of potential with all her care.

To Dr. Sofia Lima and Dr. Tânia Moniz without them, without their guidance and care for me, this project would not be possible. The word guidance never made so much sense, the loss of direction in the scientific world can be devastating for anyone but they were able to guide me when something did not go as expected. A special thanks to Dr. Tânia Moniz for supporting me every day in the lab, making me comfortable at all times to ask questions and discuss the next steps, and above all for being there for me unconditionally.

To all the members of this research group, Ana Isabel, Raquel Andrade, Andreia Marinho, Irina Monteiro, Andreia Granja, for all the help in the laboratory when that moment of doubt arose in the use of equipment or material and for all the support I felt during the months that I could consider myself part of the team.

I would like to thank CEMUP for providing the equipment to perform the SEM and confocal fluorescence analyses, especially to Dr. Rui Rocha and Professor Cláudia Nunes, respectively, who piloted the equipment and helped through all process of analysis.

Many thanks to the histology service of ICBAS for processing the skin samples for analysis. A special acknowledgement to Professor Dr. Paulo Costa, for supplying the texture analysis equipment and for his assistance during the entire procedure.

To my friends, who were able to endure my mood swings for no apparent reason gracefully and with much support. To my friends at UTAD, friends I will take with me for life, for being so different and having so much to teach me. To João Palma and Maria Francisca for all the video calls and random parties. To João Maia for worrying about the progress of my thesis and for the constant company throughout these 5 years. To Catarina Ricardo and Catarina Esquível for the perfect balance between hate and friendship within a relationship.

To my heart friends, the "manas da mama", Fernanda, Tânia, Filipa, Rita, Mariana, Maria, Carla, Rita, and Vera, for being the 9 hurricane girls with a lot to give and always ready to support in the most difficult moments. A special thanks to manas Mariana and Ritinha, for providing the best moments in the last years and for encouraging me to grow and take control of my life. Nothing better than learning that contentment does more damage than happiness.

To my family. For the support, the jokes, and the pride I can feel they have in me. Specially to my parents, Senhor Jorge and mom, for supporting me, giving me a head's up whenever it's needed, for being there. Without you, I wouldn't be who I am today. Thank you for allowing me to choose what I can do because of all the efforts you have made throughout life. To my sister, for being my mother without permission, for the jokes and headaches you give me. For the teachings a big thank you. To the little stars that were part of my life.

A huge thank you to each and every one.

Index

Acknowledgments	iii
List of figures	vii
List of tables	viii
Acronyms and abbreviations	ix
Symbols.....	x
Abstract	xi
1. Introduction	1
1.1.Dementia	1
1.2.Rivastigmine	2
1.2.1. Mode of action.....	2
1.2.2. Available formats in the market.....	3
1.2.3. Novel approaches	5
1.3.Transdermal drug delivery	7
1.3.1. Skin structure	7
1.3.2. Transdermal drug delivery strategies	9
1.3.3. Transdermal drug delivery enhancers	10
1.4.Microneedles.....	11
1.4.1. Concept and type of microneedles	11
1.4.2. Production methods	13
1.4.3. Advantages and disadvantages of a microneedle system	14
1.5.Polymeric microneedles	15
1.5.1. Marine polymers.....	15
1.5.2. Alginate	16
1.5.3. Carrageenan.....	17
1.5.4. Calcein as a model drug	18
2. Motivation	20
3. Materials and methods	21
3.1.Materials and instrumentation.....	21
3.2.Hydrogel preparation.....	21
3.2.1. Preparation of the alginate and alginate/k-carrageenan mixture hydrogel	21
3.2.2. Preparation of the drug-loaded hydrogels.....	21
3.3.Preparation and optimization of the microneedle's fabrication process	22
3.3.1. Microneedle's fabrication	22
3.3.2. Optimization process	22
3.4.Characterization techniques of microneedles	23
3.4.1. Topography analysis of the microneedles array surface - Scanning Electron	
Microscopy.....	23
3.4.2. Texture Analysis.....	24

3.5. Permeation studies - Franz Diffusion Cells	24
3.5.1. Pig ear skin preparation	24
3.5.2. Permeation study	25
3.5.3. Quantification of the drugs' permeation	26
3.5.4. Quantification of the drug remaining in the apical compartment	27
3.5.5. Skin digestion	28
3.6. Histology of the pig skin	28
3.7. Statistical analysis	29
4. Results and discussion.....	30
4.1. Microneedles: preparation and optimization process	30
4.1.1. Hydrogels' preparation.....	30
4.1.2. Microneedle's fabrication - optimization process.....	31
4.2. Calcein-loaded microneedles	33
4.2.1. Calibration curve.....	33
4.2.2. Morphology analysis.....	33
4.2.3. Texture analysis.....	36
4.2.4. Permeation assay.....	38
4.2.5. Optical and fluorescence confocal microscopy analysis	41
4.3. Rivastigmine-loaded microneedles.....	46
4.3.1. Calibration curve.....	46
4.3.2. Morphology analysis.....	46
4.3.3. Texture analysis.....	47
4.3.4. Permeation assay.....	49
5. Conclusion.....	53
6. References	55

List of figures

Figure 1 - AchE inhibitors currently used in pharmacotherapy for neurodegenerative dementia	2
Figure 2 - Schematic representation of the binding of Ach and RV to AchE	3
Figure 3 - Schematic representation of the different skin layers	8
Figure 4 - Different types of MNs	12
Figure 5 - Chemical structure of Alginate	17
Figure 6 -Chemical structure of k- Carrageenan	18
Figure 7 - Chemical structure of calcein	19
Figure 8 - Schematic representation of a texture analyser	24
Figure 9 - Schematic representation of a Diffusion Franz Cell	26
Figure 10 - Viscosity comparison between three different hydrogel formulations	30
Figure 11 - Visual aspect of 1% (w/w) calcein in alginate 7% (w/w), alginate + k-CRG 1:1 (w/w) and k-CRG 1% (w/w)	31
Figure 12 - Calibration curve for calcein	33
Figure 13 - Representative SEM images of drug-free microneedles with two needle sizes .	34
Figure 14 - Representative SEM images of calcein-loaded microneedles with two needle sizes	35
Figure 15 - Representative force-displacement curves of drug free and calcein-loaded MNs	36
Figure 16 - Percentage of permeation of calcein for porcine skin treated with free calcein, calcein-loaded hydrogels, and calcein-loaded MNs of two different heights, at different timepoints	39
Figure 17 - Apparent permeability coefficient for 3, 6, 8, and 24 hours of calcein for porcine ear skin treated with free calcein, calcein-loaded hydrogels, and calcein-loaded MNs of two different heights	40
Figure 18 - Distribution of calcein among permeated, retained, and non-permeated through the porcine skin after 24 hours	41
Figure 19 - Optical microscopy analysis of all conditions in study (H&E coloration) of the skin samples resultant from the permeation assay	43
Figure 20 - Fluorescence confocal microscopy analysis of skin samples resultant from the permeation assay	45
Figure 21 - Calibration curve for RV	46
Figure 22 - Representative SEM images of RV-loaded microneedles	47
Figure 23 - Representative force vs displacement curves for 800 μ m drug free- and RV-loaded MNs	48
Figure 24 - Representative HPLC peak of a solution containing RV	49
Figure 25 - RV permeation profile	50

Figure 26 - Apparent permeability coefficient for 3, 6, 8, and 24 hours of RV for porcine ear skin treated with Exelon®, RV-loaded hydrogels, and RV-loaded MNs 51

Figure 27 - Distribution of RV among permeated, retained, and non-permeated through the porcine skin after 24 hours 52

List of tables

Table 1 - Structural and pharmacological features of RV 5

Table 2 - Summary of MN production methods optimization 32

Table 3 - Profile of the compression forces of different MNs 37

Table 4 - Profile of the mechanical forces of drug-free and RV-loaded MNs 49

Acronyms and abbreviations

3D	Three dimensional
a.u.	Arbitrary units
AUC	Area under the curve
Ach	Acetylcholine
AChEI	Acetylcholinesterase inhibitors
AD	Alzheimer's disease
APP	Amyloid precursor protein
A β	Amyloid-beta
BBB	Blood-brain barrier
BCG	Bacillus Calmette-Guérin
BuChE	Butyrylcholinesterase
CEMUP	Centro de Estudos de Materiais da Universidade do Porto
ChEIs	Cholinesterase inhibitors
C _{max}	Maximum plasma concentration
CNS	Central nervous system
CRG	Carrageenan
DNA	Deoxyribonucleic acid
DPBS	Dulbecco's phosphate buffered saline
FDA	Food and Drug Administration
H&E	Haematoxylin and eosin
HA	Hyaluronic acid
HIV	Human immunodeficiency virus
HPLC	High-performance liquid chromatography
MN	Microneedle
NFTs	Neurofibrillary tangles
NLC	Nanostructured lipid carrier
NMDA	<i>N</i> -methyl- <i>D</i> -aspartic acid
NPs	Nanoparticles
PAMAM	Poly(amidoamine)
PD	Parkinson's disease
PDMS	Polydimethylsiloxane
PLA	Polylactic acid
PSA	Pressure-sensitive adhesive
PVPA	Phospholipid vesicle-based permeation assay
RV	Rivastigmine
SC	<i>Stratum corneum</i>

SD	Standard deviation
SEM	Scanning Electron Microscopy
SLN	Solid lipid nanoparticles
TDD	Transdermal drug delivery
T _{max}	Maximum time of drug concentration
TT	Tetanus toxoid

Symbols

κ	Kappa
λ	Lambda
ι	Iota
μ	micro

Abstract

Microneedle (MN) arrays consist of hundreds of micrometric projections arranged in a patch, capable of disrupting the skin barrier and deliver an intended therapeutic compound. Advances in microfabrication technology and the advantages of these delivery systems for cutaneous administration, comparably to oral and parental administrations, led to an increase in this research field over the recent years.

Rivastigmine (RV) is an active compound administered to patients suffering from dementia. Currently, there are two main routes of administration for this compound, oral or transdermal. However, both present limitations such as the premature metabolization of the drug, several side effects, significant drug loss, and local irritation of the skin verified for the commercially available transdermal patch, Exelon®. With all this in mind, the objective of this work is to develop and evaluate the potential of hydrogel-based MN arrays for RV delivery in a controlled manner through the skin layers.

For the preparation of MN arrays with two heights (400 and 800 μm), three different hydrogels were considered, being them alginate, k-carrageenan (CRG), and the mixture of both in a 1:1 ratio. The MN production was optimized, and a protocol was established. Calcein was chosen as a model drug for this study given the physicochemical similarities to RV. Morphology, texture, and permeation studies were performed using calcein-loaded MNs. These assays allowed to understand the behaviour of the calcein in the different hydrogels' compositions and the MNs height influence. The results show no modification in morphology for both hydrogel-based MNs however, in terms of compression force, the presence of calcein demonstrated influence in alginate MNs. Permeation studies using pig ear skin showed that the calcein release from the MNs reached a maximum value of 40% after 24 hours. Results also demonstrate the potential of 800 μm MNs for systemic delivery in comparison to 400 μm MNs given the apparent quicker release of the drug by the 400 μm MNs. Histology of the permeated skin samples was analyzed by fluorescence confocal and optical microscopy. Integration of the two imaging techniques allowed the identification of structures in the skin that appear to be caused by the perforation of the skin by the MNs.

RV-loaded systems including alginate and alginate + k-CRG 800 μm MNs were produced. Similarly to calcein-loaded MNs, morphology, texture, and skin permeation studies were performed. The morphology of the MNs appears to be maintained, yet the presence of RV influenced the compression force of MNs since both formulations experienced variation in force with alginate MNs reaching 5.74 N of compression force. Skin permeation studies revealed that RV-loaded MNs were able to reach approximately 100% of permeation after 24 hours. Apparent permeability (P_{app}) calculations are in concordance with this data. The differences between the designed systems rely mainly on the release rate. Hydrogel-based MNs demonstrated a more controlled release of drug being the more suitable option for the development of an MN patch for transdermal delivery of RV.

In the end, both alginate and alginate + k-CRG formulations exhibit suitable morphology and texture for TDD. These systems represent potential RV systemic delivery devices due to the ability of RV to pass through the skin with the majority of the drug able to cross the skin and reach the circulation with a controlled drug release profile.

1. Introduction

1.1. Dementia

Dementia is a clinical syndrome that combines a set of physical characteristics and laboratory findings caused by several underlying diseases, injuries, or infections. Progressive in nature, dementia is characterized by the deterioration of cognitive functions such as memory, judgment, thinking, comprehension, orientation, and learning leaving the patients dependent on a caregiver (Duong, Patel, and Chang 2017).

Alzheimer's disease (AD), vascular dementia, dementia with Lewy bodies/ Parkinson's disease, and frontotemporal dementia are a few of the most common forms of this syndrome, with Alzheimer's being the most common form with 60% to 70% of the cases reported. All these medical conditions have their probability of occurrence increased when faced with risk factors such as age, gender, genetics, lifestyle, among others (Denning and Sandilyan 2015).

With interest for this study, both Alzheimer's and Parkinson's disease neuropathology will be summarized.

AD is a neurodegenerative disorder characterized by the progressive loss of both cognitive and behavioral competencies. So far, the exact sequence of pathogenic events occurring in the brain remains unknown however, suppositions have been formulated (Panza, Lozupone, Seripa, *et al.* 2019). The most widely accepted hypothesis, proposed in the 1990s, is referred to as "amyloid cascade hypothesis". The baseline of this theory is the accumulation of amyloid-beta (A β) peptide, in which A β is a by-product of the amyloid precursor protein (APP) metabolism (Hardy and Allsop 1991). A β protein aggregation, starting 15 to 20 years before disease onset, results first in structures nominated oligomers that evolve over time to protofibrils, fibrils, and, finally in neuritic plaques. These structures together with intracellular deposition of neurofibrillary tangles (NFTs) of hyperphosphorylated tau interfere with the normal functioning of the brain. Neural damage and loss are also verified ensuing in deficiency of the neurotransmitter acetylcholine (ACh), important in learning and memory, driving to the eventual symptoms of dementia (Ferreira-Vieira *et al.* 2016; Panza, Lozupone, Logroscino, *et al.* 2019).

Similarly, Parkinson's disease (PD) is also caused by the destruction of brain cells. Motor features, characteristic of this disorder, are intimately related to degeneration of neurons in the *substantia nigra*, important regulators of movement in the ventral midbrain. Loss of neurons in the central nervous system (CNS) translates into dopamine depletion, alongside intra-neuronal aggregates of α -synuclein (Lewy bodies), interfering in the normal neural communication in the brain (Kalia and Lang 2015; Triarhou 2013).

Current pharmacologic treatment options for neurodegenerative dementia do not operate as a cure for the disease, as damage is not reversible, but rather to restore the disrupted neurotransmission caused by cholinergic neuron damage. Acetylcholinesterase inhibitors (AChEI) and N-methyl-D-aspartic acid (NMDA) receptor antagonists are two classes of drugs currently approved for symptomatic relief in dementia patients. Within the first group lies donepezil, RV, and galantamine, while in the second one memantine is present (Birks 2006) (Figure 1).

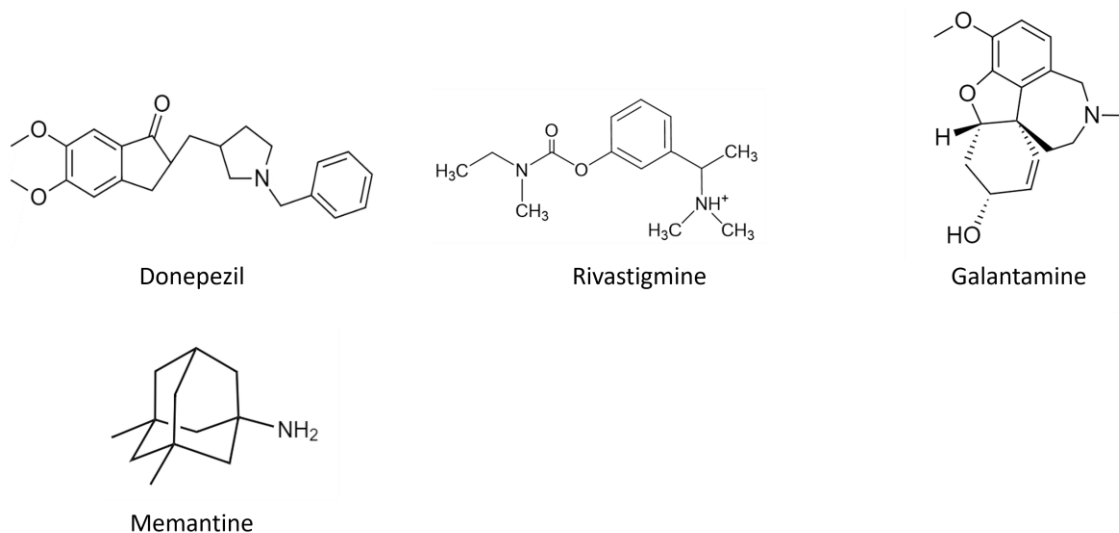


Figure 1 - AChE inhibitors currently used in pharmacotherapy for neurodegenerative dementia.

1.2. Rivastigmine

1.2.1. Mode of action

AChE inhibitors, as is the case of RV, are expected to reduce the rate of Ach degradation in the synaptic cleft. By increasing the concentration of Ach in the brain, a primary neurotransmitter, the cholinergic deficit felt is counteracted, which results in improvement of the cognitive impairment seen in patients with dementia (Birks 2006). Although employed in mild to moderate cases of dementia associated with AD (Eldufani and Blaise 2019), RV has been studied for the management of dementia non-related to Alzheimer's, as is the case of Lewy bodies dementia (Madson and Brown 2016).

RV is a carbamate-type, brain selective, and pseudo-irreversible compound. Contrary to other cholinesterase inhibitors (ChEIs), RV exhibits inhibition of both cholinergic enzymes, AChE and butyrylcholinesterase (BuChE), which presents a benefit in comparison to other inhibitors available in the market. AChE has two Ach neurotransmitter binding sites, an anionic and an esteratic site. The binding between the AChE and Ach leads to the degradation of the neurotransmitter and subsequent interruption of the signal between the presynaptic and postsynaptic neurons. Acid acetic and choline are the result products of this breakdown pathway.

RV binds to AChE in a similar manner to Ach and, promotes the "flattening" of the carbamate moiety present in the esteratic site, leading to Ach enzyme activity inhibition for over 10 hours, schematic representation can be observed in Figure 2. Given the long period of inhibition provided by this drug, RV is considered an intermediate/pseudo-irreversible agent. In the end, the drug is hydrolyzed leaving the esteratic site carbamylated and the by-products (phenolic derivative) are excreted within 2 hours (Jann 2000).

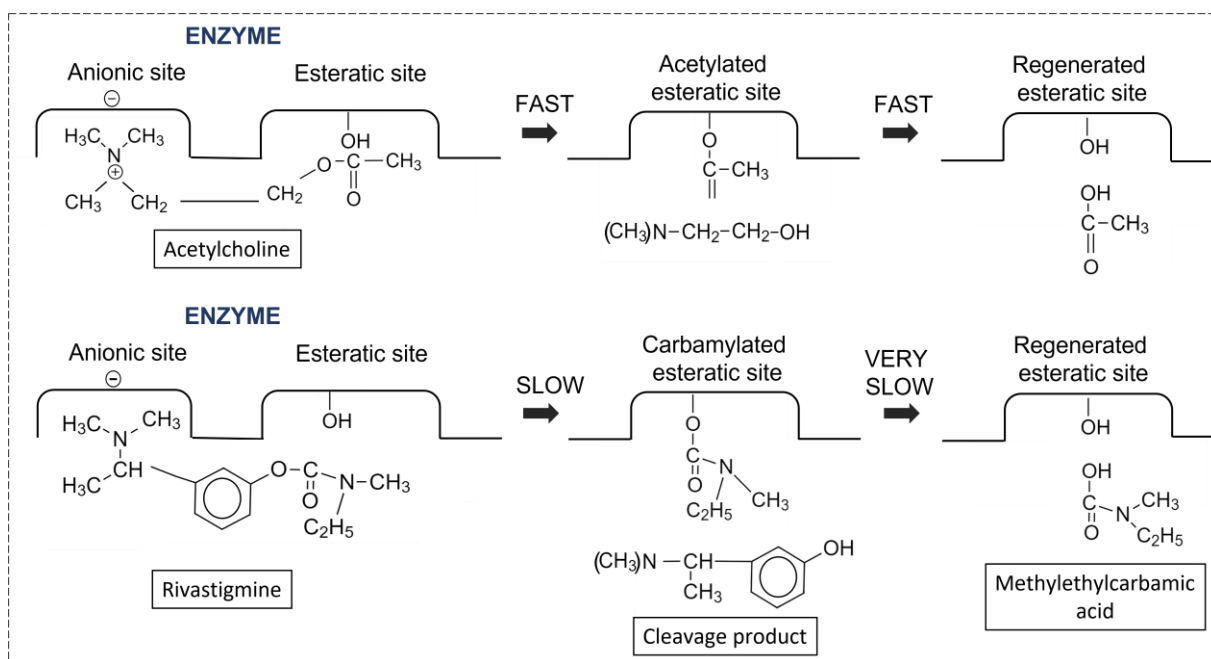


Figure 2 - Schematic representation of the binding of Ach and RV to AchE. Adapted from (Jann 2000).

1.2.2. Available formats in the market

RV, a fine crystalline powder, is available in 1.5, 3, 4.5, and 6 mg of hard capsules, administered twice a day, and a 2 mg/mL oral solution, both approved for the symptomatic control of mild to moderate dementia triggered by AD and PD¹.

Oral ChEIs are associated with side effects that may vary depending on the type of dementia for which they are being implemented. Gastrointestinal adverse effects such as nausea, vomiting, and diarrhea, particularly during drug dose adjustments, are among the most common. These side effects are, in the case of RV, directly proportional to the administered dose. Rapid maximum plasma concentration (C_{max}) of RV available in the CNS is pointed as the main responsible for undesirable effects that preclude the optimal therapeutic dose to be achieved (Sadowsky et al. 2010).

Therapeutic treatment of dementia is also formulated as transdermal patches (Exelon®) (4.6 mg [5 cm²], 9.5 mg [10 cm²], and 13.3 mg [15 cm²]) (Sadowsky et al. 2014). Exelon® transdermal patches are a single-use, prescription-only, 24 hours release patch approved in the United States for mild, moderate, and severe dementia in AD patients and

¹ Rivastigmine 1 A Pharma. (2021, April 30). European Medicines Agency. Retrieved August 20, 2021, from <https://www.ema.europa.eu/en/medicines/human/EPAR/rivastigmine-1-pharma>

mild to moderate dementia associated with PD², and approved in Europe for mild to moderately severe dementia in AD³.

The creation of a long-acting RV patch allows for the improvement of patient compliance and avoids overdosage or non-administration of the medication, especially in the elderly population (Small and Dubois 2007). However, the use of Exelon® patch requires a greater amount of drug in patch in order to obtain the intended concentration of drug in plasma (Kurz, Farlow, and Lefèvre 2009). In addition, reports show rapid drug release of RV (Chauhan and Sharma 2019) and problems associated with local skin irritation (Cummings et al. 2010).

Transdermal patches emerge as a strategy to prolong the maximum time of drug concentration (T_{max}), which means the C_{max} is achieved in a more controlled manner and create a smoother pharmacokinetic profile. The purpose of this hypothesis is to diminish the side effects felt by patients and, therefore, improve drug tolerability in the system while allowing access to maximum therapeutic doses.

RV, being a small molecule (approximately 250 Da), with both hydrophilic and lipophilic properties ($\log P = 2.45$)⁴ presents itself as an optimal candidate for transdermal release (Sadowsky et al. 2010). Table 1 summarizes the main characteristics of RV, the active compound present in Exelon® medication.

² Alzheimer's Disease | Exelon® Patch (rivastigmine transdermal system). (n.d.). Exelon® Patch. Retrieved August 20, 2021, from <https://www.exelonpatch.com/index.jsp>

³ Exelon. (2021, June 7). European Medicines Agency. Retrieved August 20, 2021, from <https://www.ema.europa.eu/en/medicines/human/EPAR/exelon>

⁴ Rivastigmine: Uses, Interactions, Mechanism of Action | DrugBank Online. (n.d.). DrugBank. Retrieved August 20, 2021, from <https://go.drugbank.com/drugs/DB00989>

Table 1 - Structural and pharmacological features of RV. Adapted from (Kandiah *et al.* 2017)

RIVASTIGMINE (ENA 713)	
Chemical name	(S)-3-[1-(dimethylamino)ethyl]phenyl ethylmethylcarbamate
Molecular formula	C ₁₄ H ₂₂ N ₂ O ₂
Molecular weight	250.34 g.mol ⁻¹
Chemical class	Carbamate derivative
Pharmacologic class	Cholinesterase inhibitor
Cholinesterase selectivity	Dual AChE-BuChE inhibitor
Formulations in the market	Capsules, oral solution, and transdermal patch
Therapeutic Indication	Symptomatic treatment of dementia in AD and PD
Adsorption	Oral: rapid and complete; Patch: lag time of 0.5 - 1h
Duration of AchE inhibition	Oral: 8-10 hours; Patch: 9 hours
Plasma half-life	Oral: 1 hour; Patch: 3.4 hours
CSF peak concentrations (cerebrospinal fluid)	1.4 - 2.6 hours
Protein binding	40% bound to plasma proteins
Bioavailability	36% for 3 mg dose

1.2.3. Novel approaches

To this day, neurodegenerative disorders such as AD and PD lack an efficient treatment, relying only on palliative nature medication, as the available care does not interrupt disease progression. Besides, the proposals that are on the market do not completely meet the patient's needs. Disadvantages either associated with side effects or with the bioavailability of the active compound itself are some of the examples. Novel therapies, given this panorama, are of the utmost importance.

A panoply of novel strategies has been established to evade the current limitations in the field. For the treatment of neurodegenerative diseases different carrier systems and different drug delivery systems, as is the case of intranasal delivery, have been explored.

Intranasal delivery of RV besides presenting itself as a practical, non-invasive delivery system, allows for a therapeutic drug to be delivered directly into the CNS via the olfactory and trigeminal neural pathways, without being exposed to the blood-brain barrier (BBB) (Hanson and Frey 2008). Circumventing the first-pass metabolism is an asset in reducing the side effects felt by the traditional neurogenerative approach, oral administration. Nanoparticles (NPs), particularly polymeric NPs, have been extensively studied for brain delivery, using polymers possessing biocompatible and biodegradable capabilities and able to increase drug adsorption in the membrane barriers due to their small size (Musumeci *et al.* 2014).

Fazil *et al.* 2012 developed RV-loaded chitosan NPs, with the intent of enhancing the bioavailability and uptake of RV through the brain. Chitosan NPs showed slower drug release when compared to the RV solution, used as a comparison in this study, and revealed a higher percentage of *in vitro* drug permeation (70.1%) compared to 20.3% of the drug solution in 24 hours. In other words, chitosan NPs showed a rapid release during the first hour (30%) followed by a slow release of drug, while the RV solution exhibited a burst release in the first 2 hours (92.54 ± 3.512 %). *In vitro* release studies proved the controlled and sustained profile of this formulation over 24 hours (Fazil *et al.* 2012). In the same sequence, Shah *et al.* 2015 reported the development and optimization of a solid lipid nanoparticle (SLN) formulation comprising RV. SLNs were tested against a standard RV solution. Among the various parameters analyzed, drug diffusion both *in vitro* using cellulose membranes and *ex vivo*, using nasal goat mucosa, appeared to be higher for the NP formulation, around 60% versus the 35% of the RV solution (Shah *et al.* 2015). Both studies validate the potential of intranasal administration of RV and the competitive value against marketed solutions for dementia.

Taking advantage of another route of administration, the parental route, Vintiloiu and co-workers developed an oleogel implant for the sustained delivery of RV. *In vivo* studies reported the release of drug for up to 11 days for one of the optimized systems composed of 10% N-stearoyl L-alanine methylester (Vintiloiu *et al.* 2007). Studies relying on intravenous administration of carrier systems were also reported (Gothwal *et al.* 2018; Ismail, Elmehad, and Salem 2013). Liposomes, as vesicular nanocarriers for the transport of RV, have shown a rapid release of the therapeutic compound, followed by a controlled release of the drug up until 24 hours, in comparison to the RV solution. The results also demonstrate great influence in the neurological department with faster memory regain (Ismail, Elmehad, and Salem 2013). Dendrimers have also been developed and tested. Gothwal *et al.* 2018 formulated RV-loaded lactoferrin modified poly(amidoamine) (PAMAM) dendrimers for delivery via the intravenous route. Enhancement on the uptake of drug by the brain (8-fold higher), as well as, lower cytotoxicity was reported, while the beneficial properties of RV were still maintained. This strategy proves to be an alternative to the available formulations suffering from low bioavailability (Gothwal *et al.* 2018).

These carrier strategies have also been implemented into transdermal patches. Lipid-based carriers, as is the case of SLN and nanostructured lipid carrier (NLC), are associated with favorable passage through the BBB, controlled release of drugs, and enhancement of bioavailability. A study developed by Chauhan and Sharma 2019 demonstrates the potential of RV-loaded NLC applied on a transdermal system to enhance bioavailability. After optimization of the formulation, NLC was composed of castor oil and glyceryl monostearate. This formulation presented a high entrapment efficiency, 70.6%, owing to the lipophilic nature of the carrier and appeared to show no irritation to the skin, contrary to the marketed Exelon® patch. Pharmacokinetics analysis also showed a slow release of the drug compared to the Exelon® patch (Chauhan and Sharma 2019). Ravic and colleagues used a transdermal film containing SLN incorporated with RV tartrate and compared this approach with a film containing the drug in the free form. Dermal toxicity studies show no significant skin reaction and the pharmacokinetic profile demonstrates improvement in bioavailability with a more controlled profile of release of the drug (Ravic, Vishal Gupta, and Balamuralidhara 2018).

A different strategy using as base a transdermal patch was developed by Cai *et al.* 2021. The proposal details the development of an RV ion paired drug-in-adhesive patch.

The optimized formulation consisting of RV associated with salicylic acid and 15% Plurol® Oleique CC 497 as permeation enhancer, and hydroxyl as pressure-sensitive adhesive (PSA) matrix. Contrary to a daily transdermal patch, this adhesive patch was intended for sustained drug delivery of 28.5 mg of drug for 72 hours. After the ion pair of PSA, the release rate of RV was visibly prolonged and controlled over time, as proven by the *in vitro* study. Ion pair strategy altered the release profile of RV given the changes in the interaction between RV and the PSA, proving to be a relevant strategy for drug delivery of this AChEI (Cai et al. 2021). Another study proposed even longer drug release within the patch for up to 6 days by means of chitosan microparticles (Sadeghi et al. 2016).

Regarding mechanisms of TDD enhancement, sonophoresis was proposed as an attractive method for the enhancement of RV permeation in the skin. This method consists of applying low-frequency ultrasound to the skin prior to RV treatment. Both permeation studies and *in vivo* studies report values of permeation and concentration of drug in plasma, respectively, more than two times the values obtained for non-treated subjects (Yu, Liang, and Liang 2015).

More recently and unique in nature when it comes to the loading of RV into MNs, a hollow MN system was developed for the delivery of RV (4.6 mg) in the liquid format through the skin. Here a 3M device is used for the delivery of the drug and is immediately removed. Authors only report the development of the device and the evaluation of the solution stability over time (Kitagawa et al. 2020).

All these novel and recent approaches highlight the relevance of this topic in the scientific community and the efforts that are being exerted to improve the current RV formulations. It should be noted that despite the encouraging results that these strategies present, nothing has yet reached the market.

1.3. Transdermal Drug Delivery

1.3.1. Skin structure

The skin is the largest organ of the human body with around 2 m² of body surface area and about 10% of all body mass (Ng and Lau 2015). Composed of various cell types and matrix components, the skin acts as a barrier against the external elements. For instance, prejudicial environmental agents such as exposure to ultraviolet light, chemical, pathogenic, and physical agents, among others (Proksch, Brandner, and Jensen 2008). Besides, and most importantly in regard to TDD, the skin functions as a site that allows the delivery of active compounds through a succession of events.

Skin is made up of three layers, the epidermis, dermis, and the hypodermis, illustrated in the Figure below, all differing significantly in their structure and function.

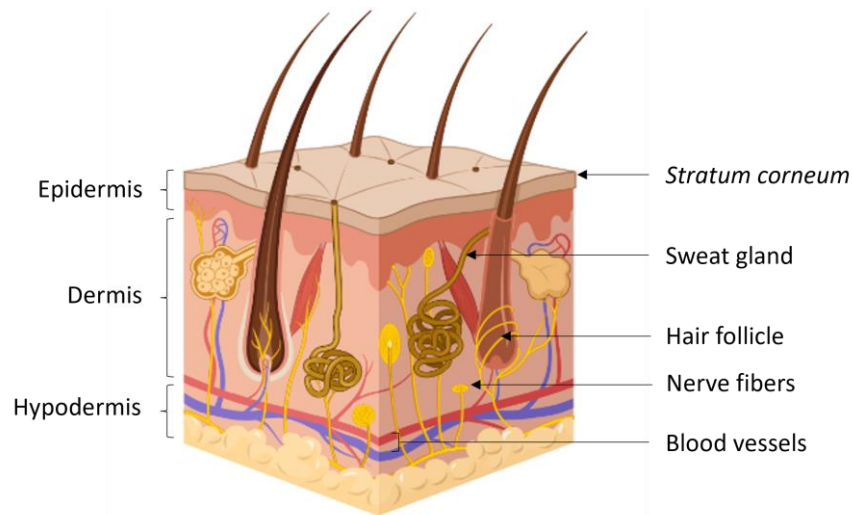


Figure 3 - Schematic representation of the different skin layers. Adapted with permission from Biorender.com.

The epidermis is the outmost barrier of the skin and consists of 15 to 20 layers of fully cornified keratinocytes, also called corneocytes. Epidermis itself is composed of four layers, *stratum basale* or *stratum germinativum*, *stratum spinosum*, *stratum granulosum*, and *stratum corneum* (SC), named from the deepest layer to most superficial layer.

Stratum basale, the innermost layer, is separated from the dermis by the basement membrane (basal lamina) connected to it by hemidesmosomes. Besides keratinocytes, this layer contains non-epithelial cells like melanocytes, Merkel cells, and dendritic Langerhans cells. *Stratum spinosum* is composed of keratinocytes, and *stratum granulosum* of keratinocytes, and a reservoir of lipids (ceramics). These three layers can also be called “viable epidermis” (Moniz, Costa Lima, and Reis 2020b; Yousef and Sharma 2018).

SC, as the uppermost layer of the skin, is the first barrier encountered by the external environment. Made up of 20-30 layers of dead keratinocytes, also known as anucleate squamous cells, embedded in a lipid matrix, is organized similarly to the “brick and mortar system”. This structure results from the turnover process of keratinocytes resulting in the accumulation of keratin and lipids. (Abdo, Sopko, and Milner 2020; Menon, Cleary, and Lane 2012).

Dermis, a connective tissue layer with 1-2 mm of thickness (Prausnitz and Langer 2008), is constituted of two layers, the papillary layer composed of loose connective tissue, and the reticular layer, a deeper and thicker sheet of connective tissue present in bundles of collagen fibers. Composed of both collagen and elastic fibers, the dermis provides flexibility, strength, and protection. Fibroblasts, responsible for the production of collagen, comprehend the majority of the cells in this layer, alongside macrophages, adipocytes, mast cells, Schwann cells, and stem cells. Hair follicles, sebaceous glands, sweat glands, sensory nerves and blood vessels, denominated skin appendages, are also present in this layer. Given the high percentage of water in the dermis, the uptake of hydrophilic drugs is preferred here (Brown and Krishnamurthy 2021; Moniz, Costa Lima, and Reis 2020b).

Hypodermis or subcutaneous layer is the innermost layer of the skin. It consists of both connective tissue, some skin appendages, and, in some sites, large deposits of adipose tissue, important in the insulation features and protection of the skin. Vascular and neural

signals are conducted through this layer (Alkilani, McCrudden, and Donnelly 2015; Yousef and Sharma 2018).

1.3.2. Transdermal drug delivery strategies

Transdermal drug delivery (TDD) concerns a non-invasive strategy in which the skin is the main delivery route for pharmaceutical drugs of interest such as topical creams, ointments, gels, sprays, or patches (Prausnitz and Langer 2008).

The penetration of a compound through the skin can occur in three distinct ways. First by the transepithelial transport route that comprises the transcellular and intercellular routes, or via the appendages. All operate in a similar fashion, firstly diffusing the drug across the SC, the first 10 to 20 μm of thickness of the epidermis, followed by the entry into the viable epidermis layer (50 to 100 μm of avascular tissue) and subsequent systemic absorption of the drug by the capillary network located in the dermis (Alkilani, McCrudden, and Donnelly 2015; Prausnitz and Langer 2008).

Painless, this method can compete with more traditional methods, namely oral administration and hypodermal injections (Ita 2020). With TDD the metabolism of molecules in the gastrointestinal tract and the first-pass effect experienced in oral administration, responsible for the low bioavailability of the medication, and consequent adverse side effects, is circumvented. Another advantage is the constant delivery of therapeutic medication. This allows for plasma drug concentration to be stable, which is beneficial especially for diseases that require systemic circulation of the drug to be continuous. Furthermore, in the particular case of systems using patches, TDD systems increase treatment compliance by patients, which can be stopped at any time by simply removing the patch (Marwah *et al.* 2016; Moniz, Costa Lima, and Reis 2021). With regards to parental drug delivery, TDD avoids the insertion of a needle that generates hazardous waste, requires the presence of a specialized professional, can cause infection on the application site, and can pose a risk for disease transmission in case of needles reuse (Prausnitz and Langer 2008).

However, in relation to patches, most of the approved systems so far only cover drugs with favorable characteristics for transdermal administration. Over 20 active compounds have been approved by the U.S. Food and Drug Administration (FDA) for transdermal delivery (Ita 2020) and over 54 transdermal patches are currently commercially available (Zhong *et al.* 2018). Some examples include drugs such as RV (Exelon®), estradiol (Estraderm®), testosterone (Testoderm TTS®), and nicotine (Nicoderm®) (Legoabe *et al.* 2010). More recently, in late 2019, asenapine, an antipsychotic drug of the second generation, was approved for the treatment of patients suffering from schizophrenia under the commercial name Secuado® in the form of transdermal patch. Similar to what happens with Exelon®, three different dosages were developed (Carrithers and El-Mallakh 2020).

All candidates mentioned, in order to be suitable for TDD, require low molecular weight (500 Da), lipophilic behavior, and be able to generate therapeutic effect in low doses (in the milligram or microgram range) (Ita 2020; Prausnitz and Langer 2008). Obeying these requirements has as a consequence the limitation in the number of drugs suitable for TDD. Also, since it is a patch that stays in prolonged contact with the human body, reactions such as itching, redness, burning, or a stinging sensation can act as a limiting

factor. This can happen due to skin sensitivity inherent to a population group or by the therapeutic medication itself (Ita 2020).

TDD demonstrate advantages over both oral and parental drug delivery, nonetheless, advances in this area are necessary to overcome the limitations still present. As mentioned, the reduced number of suitable drugs for TDD as well as the restriction on the dosage implemented in each delivery system are some of the weaknesses associated.

1.3.3. Transdermal drug delivery enhancers

TDD can be divided into three generations. Concerning transdermal patches presently available on the market, the majority fall into the first generation. These devices are based on the delivery of molecules able to cross the skin barrier without the need for enhancement agents, i.e., drugs with naturally suitable characteristics for TDD (Ita 2020; Prausnitz and Langer 2008). In this passive delivery route, the principle of Fick's law of diffusion is considered, where the therapeutic molecules cross the skin while a concentration gradient is present (Subramony Anand 2013).

Contrarily, the second generation of TDD systems forces a temporary and reversible disruption of the SC barrier which allows for more efficient delivery, without compromising the deeper tissues. Within this category, both passive and active approaches are reported. Ion pairing, chemical enhancers, electrically assisted methods (iontophoresis and ultrasounds), liposomes, and NPs are some of the examples present in this category (Prausnitz and Langer 2008). Referred to as a passive approach, the use of chemical enhancers is one of the most used techniques for the improvement of skin permeation. The reversible disruption of the SC can be achieved by numerous mechanisms such as increasing fluidity of the lipidic layers, inducing disruption of the intercellular lipids, hydration of the SC, and alteration of the thermodynamic properties of the drug.

Iontophoresis, a second-generation active approach, is defined by the application of small electric currents with the intent to enhance the transdermal delivery of ionizable drugs, mostly. Nevertheless, both strategies present limitations. Chemical enhancers due to the relationship between the concentration of the chemical and skin irritation phenomenon's, and, the second method, given the possible current-induced damage caused in the skin (Alkilani, McCrudden, and Donnelly 2015; Ramadan *et al.* 2021).

Del Rio-Sancho *et al.* 2012 report the benefits of both chemical enhancers and the application of iontophoresis with low ionic strength in the administration of memantine, used in AD patients, transdermally. R-(+)-limonene, a compound pertaining to the terpenes class, functioning as an enhancer, showed enhanced TDD for the targeted drug with a flux value of $91.9 \pm 8.2 \mu\text{g}/\text{cm}^2 \text{ h}$. Nevertheless, when comparing results, iontophoresis appears to be superior to any chemical enhancer used in this study (Del Rio-Sancho *et al.* 2012). Given the specific effect of each TDD enhancer technique, it is possible to observe in the literature the use of more than one method simultaneously, as is the case of Datta, Panchal, and Venuganti 2021, which uses chemical enhancers alongside techniques like iontophoresis and tape stripping for the delivery of a peptide antibiotic (Datta *et al.* 2021).

Drug delivery that triggers a strong disruption of the SC, by either partial interruption or removal of the outmost layer skin barrier comprises the third generation of TDD devices. Delivery of macromolecules (deoxyribonucleic acid (DNA) and proteins), small molecules, and vaccines are some of the possibilities thanks to the development of strategies like the

combination of chemical and biochemical enhancers, electroporation, thermal ablation, and more recently, MNs, among other physical methods (Prausnitz and Langer 2008).

MNs, discussed in detail in the next section, are of particular interest in this study. MNs are a minimally invasive mechanical approach for the enhancement of drug permeation. These arrays can vary in shape, length, width, and material. The purpose of these devices is to deliver the drug by penetrating the SC without tissue damage and in a painless manner (Alkilani, McCrudden, and Donnelly 2015; Chen *et al.* 2020).

1.4. Microneedles

1.4.1. Concept and type of microneedles

A MN drug delivery system consists of hundreds of microscopic projections arranged in a patch, with competencies to temporarily disrupt the skin barrier. These structures create micron-sized pores, larger than the molecular size, in the upper layers of the skin and permit the delivery of compounds such as hydrophilic macromolecules, as well as supramolecular complexes and microparticles, directly into the systemic circulation (Donnelly, Singh, and Woolfson 2010).

The design of the MN device is crucial for the efficient performance of the system. A MN device should be able to reach the epidermis or upper dermis layers without system breakage or buckling. At the same time, needs to avoid contact with nerve fibers and blood capillaries while allowing the creation of an adequate pathway for drug delivery (Alkilani, McCrudden, and Donnelly 2015). Although the dimensions may vary, for example, depending on the type of application, MNs normally feature 25 to 1500 μm in height, 50 to 250 μm in base width, and 1 to 25 μm in tip diameter. Concerning the shape, needle tips are available in many formats, like triangular, cylindrical, or pentagonal (Waghule *et al.* 2019).

Five categories of MNs are recognized as strategies for TDD, based on the delivery profile. Figure 4 shows the different types of MNs and the overall process of application and removal of the device.

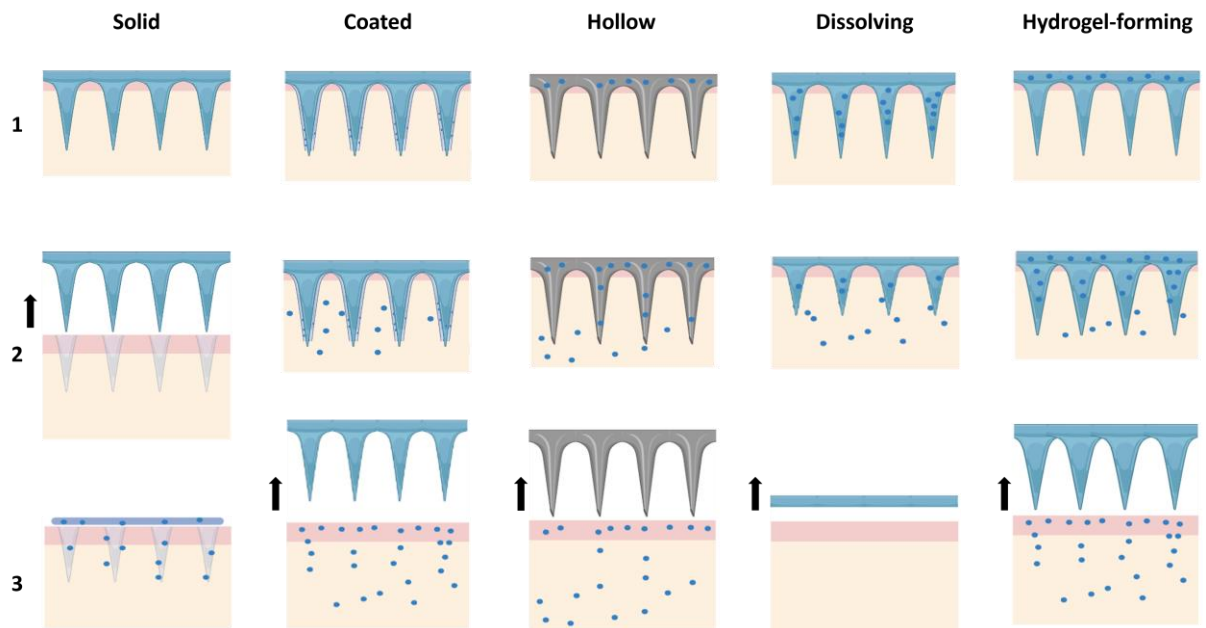


Figure 4 - Different types of MNs. 1-Application of the MN; 2- Release of the drug from the system (dots); 3-Removal of the device (arrows). Solid MNs have in step 2 the removal of the device.

Solid MNs are micrometric needles made of a rigid material and are often used for the treatment of the skin prior to the administration of the therapeutic compound. The microchannels formed allow for the passive diffusion of molecules through the skin. Since skin regeneration counteracts the permanence, for long periods of time, of these channels in the skin, the drug is usually delivered through a patch. This system is described as the “poke and patch” principle (Waghule *et al.* 2019).

Coated MNs, as the name implies, consists of a MN as the base with a coating of a given drug solution/dispersion (Ita 2020). The two-step system required by the previous MN type, where first the MN creates the pores and secondly the active compound is applied, is bypassed with this strategy. For this type of MN, the drug is delivered quickly. Although appealing for the delivery of high molecular weight molecules, the amount of drug that can be loaded onto a coated MNs is dependent upon the size and width of the MN. Generally, this type of MN presents low drug loading capacity due to the reduced surface area available (Alkilani, McCrudden, and Donnelly 2015).

Hollow MNs, “poke and flow”, resemble hypodermic needles, having a solid exterior with an empty space or lumen. It’s here that large amounts of a drug are stored until it can be released either by passive diffusion or with the help of a driving force so as to increase the rate of delivery, and the overall quantity of drug delivered (Roxhed *et al.* 2008). Nonetheless, given the complex architecture, hollow MNs require precise and expensive technology for production (Hong *et al.* 2014).

Dissolving MNs function according to the type of material with which they are formulated, normally polymers (Ita 2015). After insertion into the skin, and depending on the trigger stimulus, the drug dissolved in the biodegradable material is released. Drug delivery is made in a controlled manner which poses benefits, especially for long-term drug delivery therapies. Due to the dissolution of the compound in the skin, the MN system is not removed after insertion as it occurs with solid MNs.

Given the simplicity of the mechanism in question, as opposed to solid or hollow MNs, fabrication is a simpler process. Moreover, the “poke and release” procedure only requires a one-step application, which is beneficial from a practical point of view (Waghule *et al.* 2019). According to the literature both low and high molecular weight molecules can be delivered with this method (Alkilani, McCrudden, and Donnelly 2015).

The fifth category, hydrogel-forming MNs, have been considered an independent set of MNs. While dissolving MNs dissolve the compound after MN placement, this system consists of swelling polymers. Both methods represent a bio-responsive system. First, upon insertion, the needles allow for the disruption of the SC. When in contact with interstitial fluid, the polymers swell and open the channels created upon insertion of the MN system. This mechanism allows a controlled drug release rate (Moniz, Costa Lima, and Reis 2021; Waghule *et al.* 2019). Upon removal of the device, the overall structure of the needles is kept intact (Donnelly *et al.* 2013).

MNs can be further classified in line with the type of material they were formulated. There are polymeric options, which include biodegradable and non-biodegradable polymers, and non-polymeric options such as ceramics, glass, and metals (Moniz, Costa Lima, and Reis 2021; Nagarkar *et al.* 2020).

1.4.2. Production methods

The fabrication method selected for MN production depends on various factors, such as the type, geometry, and material of each MN (Waghule *et al.* 2019). Several techniques are described in the literature for the production of MNs, however, micromoulding (Park *et al.* 2007), laser cutting (Gill and Prausnitz 2007), lithography (Pérennès *et al.* 2006), and wet and dry etching (Maldonado Loyo and Niño De Rivera Y Oyarzabal 2011) are some of the most common.

Micromoulding is a mold-based approach where a micromould, generally composed of polydimethylsiloxane (PDMS), is produced, and utilized as a negative mould (Indermun *et al.* 2014; Moniz, Costa Lima, and Reis 2021). PDMS constitutes an excellent option among plastic materials given the durability of the material since it can be used an infinite number of times and the fact that it is transparent and affordable (Park *et al.* 2007). The material that makes up the MN is reduced to a liquid or semi-liquid state into the micromould and is, subsequently solidified to acquire the intended form (Yao 2009). Both dissolving and ceramic MNs employ PDMS micromoulds. The fact that it is a low-cost, simple process with capacity for mass production makes this technique commercially attractive (Park *et al.* 2007). As insufficient wetting of the moulds or high viscosity of the material can compromise the penetration of the compound into the mould, which means the MNs are produced with imperfections. Some additional steps, as vacuum and centrifugation procedures, can be applied to avoid mechanically poor MNs. In the end, MNs are dried and demoulded (Moniz, Costa Lima, and Reis 2021; Shravanth *et al.* 2021).

Laser cutting or laser ablation is used for metal and polymeric MNs and is based on the application of a laser beam directly into the mould to create the intended format. Aoyagi *et al.* 2007, for example, used a KrF laser beam to introduce holes into a polylactic acid (PLA) MN, previously produced by a micromoulding technique. Viability was confirmed through the introduction of the hollow MN into blood plasma and posterior uptake of blood

by the needle (Aoyagi *et al.* 2007). Although being an impressive manufacturing technique, it requires trained personal and is not cost-efficient (Shravanth *et al.* 2021).

Drawing lithography is a well-established technique applied for the production of stamps/micromoulds. It concerns a mold-free technique, where the glass transition properties of a polymer are taken advantage of to produce MNs. A viscous polymer is placed in a plate, while another plate contacts with the glassy liquid polymer and in a controlled fashion pulls away, causing deformation of the polymer structure and forming the desirable design (Lee and Jung 2012; Moniz, Costa Lima, and Reis 2021).

Even though micromoulding is the most common methodology, techniques like dip coating for coated MNs, master mould production due to electroplating for solid MNs, or injection moulding for dissolving MNs are a few more examples described in the literature (Shravanth *et al.* 2021).

1.4.3. Advantages and disadvantages of a microneedle system

As one of the most promising approaches for the improvement of TDD, MNs allow the delivery of an active therapeutic compound competently, while overcoming some of the limitations presented by conventional systems, such as topical creams, transdermal patches, or hypodermic needles (Waghule *et al.* 2019).

Both topical creams and transdermal patches present low bioavailability given the necessity of the compound to be able to cross the SC. Although enhancers can be added, the improvement in drug permeation is not considerably higher (Waghule *et al.* 2019). On the other hand, hypodermic needles, as mentioned before, represent a painful approach with hampers patient compliance (Prausnitz and Langer 2008). Advantages already described for TDD are common to the MN devices as is, for example, the minimal invasiveness and the ease of administration and disposal. Besides, the temporary micron-sized pores generated, permit delivery of the drug at the same time as reducing the probability of infection caused by pathogens, in comparison to hypodermic needles. However, the manner in which the SC barrier is disrupted is one of the differences between the several TDD approaches and MNs.

Even though TDD enhancers can disrupt the SC layer, the dimension of the pores created is smaller than the ones generated by MNs. Given that, a larger number of pharmaceuticals and cosmetics can be delivered using MNs which expands the number of drugs suitable for transdermal delivery. As a huge number of new drugs with biological origin are emerging, this methodology is very beneficial (Alkilani, McCrudden, and Donnelly 2015). Insulin is a perfect example of a macromolecule that is unable to passively cross the skin barrier, relying on alternatives such as MNs for drug delivery, given the vast advantages associated (Xie, Li, and Yu 2015).

MNs perforate the skin layers and deliver the intended drug in the dermal layer, characterized by the abundant presence of blood and lymph vessels. Owing to the accessibility to an immune-competent organ, the use of MNs in the context of vaccination or treatment of immune system-related diseases has been attracting attention (Leone *et al.* 2017). Vaccine formulations, using MNs as the delivery system, against human immunodeficiency virus (HIV) (Zaric *et al.* 2017), influenza (Frew *et al.* 2020), and even the new coronavirus (SARS-CoV-2) (Kim *et al.* 2020) are some of the many examples described in the literature, that present exciting results. The fact that MNs combine the

benefits of TDD systems and still allow circumventing the major limitation associated with the size of the molecules, renders MNs an attractive approach in the scientific field, proven by the increasing number of studies over the last few years ⁵.

Nevertheless, despite the advantages listed there are still some concerns about the use of these delivery systems. The insertion of a MN array opens the way for bacterial and fungal activity which can cause inflammation of the tissue. In addition, the increase in drug concentration under the dermis can also cause skin sensitivity/irritation (Indermun *et al.* 2014). Although not applicable for all MN types, the application of the device requires trained personal and adequate characteristics of the MN, in order to avoid MN breakage or buckling. Stainless steel, for example, characteristic of solid MNs, is only intended for the creation of skin pores and immediate removal. When placed for long periods of time in contact with the skin, due to mechanical failure, skin inflammation can be observed (Indermun *et al.* 2014; Li *et al.* 2017). Another disadvantage is the unpredictable manner in which the system works, that is, the use of this type of system does not always guarantee that the therapeutic drug concentration will be reached (Ita 2015).

1.5. Polymeric microneedles

1.5.1. Marine polymers

As stated previously, a range of materials can be used as constituents for the manufacturing of MNs, among them are ceramics, glass, metals, and polymers (Nagarkar *et al.* 2020).

Polymers represent a biocompatible, versatile, cost-efficient, and easy-to-produce alternative to the remaining materials. Although glass and silicon are more abundant within the microelectronics industry, the production of MNs using these materials makes the overall process more expensive. On the other hand, even though metals are more appropriate for MN fabrication when compared to polymeric systems, regarding their mechanical strength, they represent a less cost-efficient option (Lee, Han, and Park 2013).

Many biocompatible, biodegradable, and water-soluble polymers have been studied as drug delivery systems given their high loading capacity of drugs within the polymeric matrix. Drug loading within the polymeric MN facilitates the controlled release of a given biopharmaceutical product, the prospect of targeting specific tissues, and the ability to respond according to different stimuli (Singh *et al.* 2019). Furthermore, granted the viscoelastic properties presented by polymers, mechanical strength related to shear breakage is enhanced (Lee, Han, and Park 2013).

In light of the relevance to this study, the benefits associated with marine-based polymers, particularly polysaccharides, will be explained.

⁵ Microneedles - Search Results. (n.d.). PubMed. Retrieved August 25, 2021, from <https://pubmed.ncbi.nlm.nih.gov/?term=Microneedles>

Marine polysaccharides, obtained from algae, animals, and microorganisms, represent a sustainable, cheap, and non-toxic source of polymers that preserve the beneficial features of biodegradability and biocompatibility like the remaining polymers. Additionally, these polysaccharides can exhibit anti-inflammatory and antimicrobial properties (Barbosa *et al.* 2019). Regarding chemical structure, natural polymers result from the condensation between monosaccharide units joined by glycosidic linkages (Barbosa *et al.* 2019).

The most pertinent marine-origin polysaccharides for this particular study are alginate and k-CRG, although many other polymers like chitosan and hyaluronic acid (HA) manifest relevance within the scientific community as drug delivery systems (Moniz, Costa Lima, and Reis 2021).

1.5.2. Alginate

Alginate (alginic acid), whose chemical structure is represented below (Figure 5), is a natural source, anionic and biodegradable polysaccharide isolated from brown seaweed (*Phaeophyceae*) and available in the market in different formulations.

Alginic acid consists of D-mannuronic and L-guluronic acid residues arranged randomly in blocks in the polymer chain. The mannuronic to guluronic ratio within the polymeric chain will affect the properties of the alginate gel formed, like swelling, and viscoelasticity. For instance, alginates with a high content of guluronic acid blocks, comparably to richer mannuronic alginate, presents alginates with a higher strength as a result of the affinity of guluronic acid residues to divalent ions (Tønnesen and Karlsen 2002).

Alginate and its derivatives have been applied in the cosmetic and food industry. However, the potential of alginate to function as a controlled and tunable drug delivery system is of great importance attending to the capacity of this polysaccharide to retain water molecules inside its matrix, leading to a high viscosity “acid gel” upon hydration of the alginic acid (Moniz, Costa Lima, and Reis 2021; Tønnesen and Karlsen 2002). Plus, owing also to the organized, ordered, and stable structure that natural polymers present (Qureshi *et al.* 2019). Despite the various transport systems in which this polysaccharide can be included, it should be noted that its use in MNs has been attracting attention. A pertinent example of the alginate applicability in MN formulations is the work developed by Arshad and colleagues (Arshad *et al.* 2020). In an attempt to replace the adoption of the conventional drug delivery system in the vaccination procedures, a Bacillus Calmette-Guérin (BCG)-loaded MNs system was formulated coupling the use of sodium alginate, as a permeation enhancer, and trehalose. Examining the immune response of the *in vivo* model revealed an improved humoral immunity which proves the effectiveness of the MN patch as a painless vehicle (Arshad *et al.* 2020).

Alginate MNs are also giving the first steps in the management of diabetes. Chen *et al.* 2017 developed an alginate-based MN patch loaded with two types of mineralized particles, exendin-4, and glucose oxide. The self-regulated system demonstrated adequate response by inducing a normal glucose level in case of hyperglycemia. Interestingly, the introduction of the particles improved the mechanical properties of the patch without compromising drug release (Chen *et al.* 2017).

Both examples demonstrate the important properties of alginate as a drug delivery system.

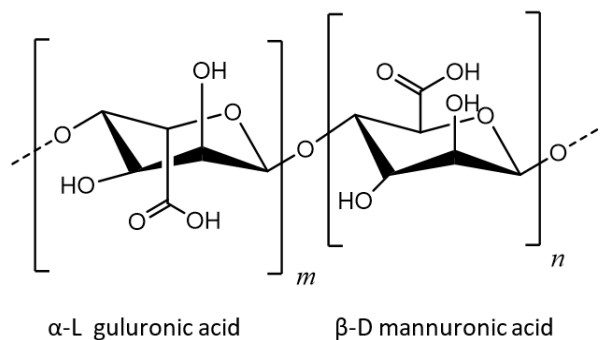


Figure 5 - Chemical structure of Alginate.

1.5.3. Carrageenan

CRG, viewed in Figure 6, is a natural source, anionic and linear sulfated polysaccharide extracted from the cell wall of red seaweeds. This polysaccharide is comprised of alternated units of D-galactose and 3, 6-anhydro-galactose joined together by α -(1 \rightarrow 3) and β -(1 \rightarrow 4) glycosidic linkages. Sulfation of the moieties is responsible for the negative charge of CRG polymers (Qureshi et al. 2019).

Many different structures of CRG have been identified, however, κ (Kappa), λ (Lambda), and I (Iota) CRG are the most relevant commercially. These formulations can be distinguished from each other by the degree of sulfation, source, position, and number of sulfate groups.

In general, CRG polymers present biocompatibility, the ability to interact with other polymers, biodegradability, low toxicity, and low cost, certifying their importance in both the food and pharmaceutical industry. In the food industry, similar to what happens with alginate derivatives, works as a thickener, gelling and stabilizing agent (Qureshi *et al.* 2019). Moreover, CRG demonstrates appealing characteristics for encapsulation of bioactive compounds by improving compound retention and due to the ability to protect the therapeutic substance from degrading agents (Dong, Wei, and Xue 2021). Besides that, anticoagulant, antithrombotic, antiviral, anti-cancer, and immunomodulatory properties, among others, can also be associated with this polysaccharide (Qureshi *et al.* 2019). Plus, anti-inflammatory properties have been linked with CRG (Kim *et al.* 2019). As a thermo-reversible gel formation compound, CRG is soluble at high temperatures (above 60°C) and, when the temperature drops to around 30°C physical gelation occurs.

k-CRG, the type of CRG used in the formulation of the MNs developed in this work, is composed of alternating α -(1 \rightarrow 3)-D-galactose-4-sulfate units combined to β -(1 \rightarrow 4)-anhydro galactose residues. When in gel form, a secondary helical structure is acquired (Qureshi *et al.* 2019). So far there is no record of MNs produced with this polysaccharide.

In this work, by mixing two hydrogels in different proportions, the mechanical properties of the system can be changed, making them more suitable for a given function.

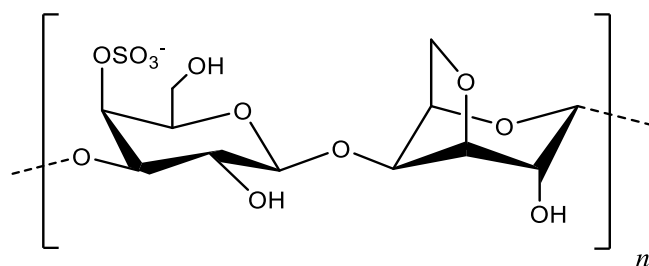


Figure 6 -Chemical structure of *k*-Carrageenan.

1.5.4. Calcein as a model drug

A model compound is often considered in the first steps of an experimental layout, during the design of a drug delivery system. It may possess characteristics comparable to the drug that is intended to be delivered and is used aiming to characterize the performance of the developed delivery system.

Calcein, 4',5'-bis[N,N-bis(carboxymethyl) aminomethyl] fluorescein, represented below, is a hydrophilic, polyanionic, and low molecular weight (622.55 Da) molecule. Working like a fluorescent dye, calcein can be easily detected through ultraviolet-visible and fluorescence spectroscopy (Oh *et al.* 2008).

As a drug model, calcein is often used in the evaluation of the permeation of different systems. Phospholipid vesicle-based permeation assay (PVPA) is an *in vitro* lipid model applied in the scientific field for the evaluation of passive diffusion of compounds in various settings.

Shakel and colleagues report the development of a modified PVPA model resembling the composition of the human SC and the subsequent evaluation of permeation. Here, calcein was employed in order to evaluate the permeation profile of the newly developed system and, coupled with five different drugs, to verify the stability of the barrier when exposed to selected drugs (Shakel *et al.* 2019). Based on this work, Moniz and partners used the abovementioned barriers and evaluated a set of parameters against the *ex vivo* pig skin model. The storage stability of the PVPA barriers, the influence of pH in the permeation of a drug, and the influence of co-solvents were some of the performed tests in which calcein functions as the permeation drug (Moniz, Costa Lima, and Reis 2020a).

Seeking to characterize novel MN devices, Oh *et al.* 2008 reported the design of a solid MN, particularly biocompatible polycarbonate MNs, loaded with calcein. For this research, calcein functioned as a skin permeation agent, allowing for the quantification of the compound that was able to cross the skin layers. Furthermore, the way calcein gel would be more adequately delivered, the length, and the density of an MN were also evaluated. The goal was to develop a TDD system capable of delivering hydrophilic compounds, generally considered impermeable. The report shows enhanced permeability of calcein using MNs (Oh *et al.* 2008). Another study also reported the use of two model dyes, one of which calcein, to assess skin permeation printed MN arrays (Xenikakis *et al.* 2019).

The examples explained above demonstrate the importance of calcein in the evaluation of skin permeation studies.

In the present work, calcein will act as the model drug to characterize the permeation profile of drug loaded in the MNs that will be produced to deliver RV through the skin. This drug is the candidate herein proposed for the drug delivery system.

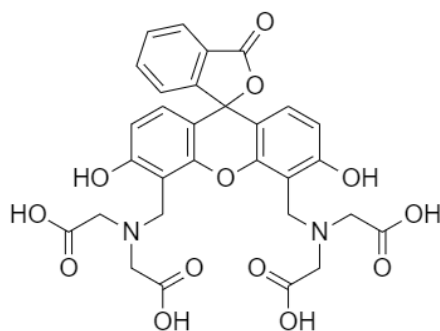


Figure 7 - Chemical structure of calcein.

2. Motivation

The goal of this study was the development of an MN array capable of systemic delivery of RV through the skin in a controlled manner, to improve dementia therapeutic options available today. The study comprises the use of two types of hydrogels made from natural polymers, alginate and k-CRG, and two types of MN moulds with different heights - 400 μm and 800 μm .

The evaluation of the ability of the hydrogels to produce MN arrays capable of piercing the skin, as well as the evaluation of their behavior in drug permeation are essential parameters of the study. In order to produce, characterize and evaluate the performance of the arrays, a variety of sets and techniques were required for the development of this thesis.

Firstly, the production and optimization of the MNs' fabrication process that would allow an appropriate MN array was pursued. Secondly, the characterization of the MNs produced by 3 different formulations in study using morphological analysis (SEM), with the intent to evaluate the capability of the formulations to produce MNs with the desired shape. Next, the production and characterization of calcein-loaded MNs, namely alginate and alginate + k-CRG hydrogels through morphological analysis of the MNs using SEM and the evaluation of their compressive strength, employing a texture analyzer, in comparison with drug-free MNs. With the aim of assessing the suitability of the different MNs systems as TDD, the skin permeation profile was attained.

Once the optimization and selection process was finished, RV-loaded MNs were formulated and characterized using the optimized techniques defined above for calcein-loaded MNs. This research study will allow the evaluation of new delivery systems for RV to overcome drawbacks associated with currently available solutions.

3. Materials and methods

3.1. Materials and instrumentation

Sodium alginate was purchased from ACROS Organics™ (Thermo Fisher Scientific, Massachusetts, USA). Calcein, k-CRG, RV tartrate, and Dulbecco's phosphate buffered saline (DPBS) (10x) were acquired from Sigma-Aldrich (St. Louis, MO, USA). Exelon® patches were acquired from Novartis. Acetonitrile was acquired from Fisher Scientific (Hampton, EUA). Silicone moulds were obtained from Micropoint Technologies (Singapore). The porcine ears were purchased in a local slaughter (Porto, Portugal). Double-deionized water was provided by an ultra-pure water system (Arium Pro, Sartorius AG, Gottingen, Germany). The reagents were weighted in a digital analytical balance Kern ACJ/ACS 80-4 (Kern & Sohn; Balingen, Germany). pH measurements were achieved using a JENWAY 550 pH meter (UK). SEM and confocal studies were performed at "Laboratório de Microscopia Eletrónica de Varrimento e Microanálise por Raios X" and "High-Resolution Microscopy Unit", respectively, both at CEMUP ("Centro de Estudos de Materiais da Universidade do Porto"). Histological samples have been processed in the histological service of ICBAS, Universidade do Porto.

3.2. Hydrogel preparation

3.2.1. Preparation of the alginate and alginate/k-carrageenan mixture hydrogels

Two different kinds of polymers, alginate, and k-CRG, were chosen for this study given their biocompatibility, biodegradability, and non-toxic properties (Moniz, Costa Lima, and Reis 2021; Qureshi *et al.* 2019).

Alginate and k-CRG solutions were prepared by dissolving the alginic acid and k-CRG powders in double deionized water at a final concentration of 7% and 1% (w/w), respectively. Solutions were placed in a magnetic stirring plate (IKA-Werke, Staufen, Germany) at 60°C, under continuous stirring, until a homogeneous solution was obtained. After that, the polymers were allowed to cool down before preparing the mixture of alginate and k-CRG, obtained by weighing and physically mixing the two polymeric solutions in the proportion of 1:1 (w/w).

3.2.2. Preparation of the drug-loaded hydrogels

As mentioned in the introduction, the model drug used in this study was calcein, a fluorescent compound. Calcein, at a concentration of 0.1% (w/w) was initially added to each hydrogel formulation, mixed with a spatula and then, placed into a sonication bath

(Sonica® Ultrasonic Cleaner) for a few minutes to ensure all calcein molecules were incorporated into the hydrogel. Once the three mixtures were prepared, aluminum foil was used to protect the samples from the light.

RV-loaded hydrogels were produced in the same manner, taking into account the mass of RV per cm² of Exelon® patch. Considering a uniform distribution of RV in the patch, Exelon® Patch 5 cm² presents 1.8 mg of drug per cm². The microneedles present 0.5 cm² of area, which translates into the addition of 0.9 mg of RV per MN array in this study (0.9 mg/150 mg hydrogel).

3.3. Preparation and optimization of the microneedle's fabrication process

3.3.1. Microneedle's fabrication

Microneedles were produced using a silicone MN mould. For this investigation study, two different types of moulds were attained, differing on the height and base of the needle. All MN moulds have a total of 100 MNs, which translated into an array of 10 x 10. MNs pyramid base has 150 or 200 µm and a height of 400 or 800 µm, respectively.

After the preparation of the three hydrogels (alginate, k-CRG, and alginate + k-CRG), 50 mg of each was loaded into the respective microneedles' moulds and then placed in a 12 well plate. Following, the MN molds were centrifuged (Eppendorf centrifuge, 5810R) at 3500 rpm and 30°C for 1 hour. After being processed, the molds were kept overnight in a climate room at 21°C, in a Petri dish sealed with parafilm and protected from the light. On the second day of MNs production, a second layer of 150 mg of polymer was added to the molds, followed by centrifugation in the same conditions mentioned above but, this time, for 2 hours.

For the drying process, the filled molds were placed in the incubator shaker (ES-60 Incubator Shaker, Miulab, Hnagzhou, Zhejiang, China) at 100 rpm and 25°C for 3 hours or until the corners of the MNs appear to be detaching from the MN mold. The protocol was adapted from Chen *et al.* 2012.

3.3.2. Optimization process

MN production applying the method mentioned in section 3.3.1 was inefficient given the loss of polymer that was observed after each centrifugation cycle (discussed in section 4.1.2).

A second protocol was developed, this time the amount of polymer was reduced to a total of 150 mg. In the first layer, 100 mg of polymer was added and centrifuged at 2500 rpm at 30°C for 30 minutes. The second layer, added with a period of 24 hours between layers, consisted of 50 mg of polymer, followed by centrifugation at 500 rpm at 15°C for 15 minutes. The drying process in the incubator shaker, on the third day of MN production, had a duration of 3 hours at 150 rpm at 25°C with fan.

The third attempt of optimization was composed of 50 mg of polymer on the first day and, subsequent centrifugation of the MNs molds at 500 rpm at 15°C for 15 minutes. On the second day of MN production, 100 mg of polymer was added under the same conditions as the first layer. On the third and final day, MN templates were incubated for 2 hours at 25°C, in the incubator shaker, first at 150 rpm which was later increased to 250 rpm in an attempt to remove air bubbles still present and to let the polymer sink into the MN mold cavities. Next, the MNs were centrifuged for 1 hour at 500 rpm at 10°C and, finally dried at 150 rpm at 25°C for 3 hours.

The fourth and final protocol developed was based on a 4-layer process, and the MN molds were only displayed in the middle row of the 12 well plate since it was observed less polymer loss when in this location. On the first day, 25 mg of polymer was added to each mold and centrifuged at 3500 rpm, 30°C for 1 hour. Next, a second layer of 25 mg of polymer was placed on the surface of the mold and the same conditions were applied. On the second and third days, the amount of polymer per mold increased to 50 mg and the treatment conditions were kept. For the drying process, the filled micromoulds were placed in the incubator shaker at 150 rpm and 25°C for 3 hours or until the corners of the MNs appear to be detaching from the MN mold. Finally, the MNs were demolded using regular adhesive tape. In the end, MNs were obtained with 150 mg of polymer and with no significant losses observed.

For the following studies, only this method has been considered to produce MNs.

Empty MNs (without any compound) of each hydrogel mixture have been prepared as the control for morphological and texture analysis.

3.4. Characterization techniques of microneedles

3.4.1. Topography analysis of the microneedles array surface - Scanning Electron Microscopy

The surface morphology of the fabricated MNs was visualized by SEM using a FEI Quanta 400 FEG ESEM/EDAX Pegasus X4M with an accelerating voltage of 10kV for high-resolution imaging. MN arrays were mounted onto metal pins with double-sided carbon tape and coated with an ultra-thin layer of gold/palladium (Au/Pd), to increase surface conductivity.

Drug-free MNs, calcein-loaded, and RV-loaded MNs were observed using a magnification of 75x and 250x to get a general image of the patch and a more detailed look at the needle structure, respectively.

3.4.2. Texture Analysis

In order to determine the compression force for each type of MN, mechanical characterization was performed using a TA.XT2 Texture Analyser (Stable Micro Systems Ltd., Haslemere, UK).

MNs were placed on a flat rigid surface of a stainless-steel base plate and an axial compression load was applied through a metal probe of 2 mm of diameter moving towards the baseplate with a 0.3 mm path length, at 0.01 mm/s (Figure 8). For each MN device, at least 5 readings were made, one in the central part of the MN array and one at each vertex.

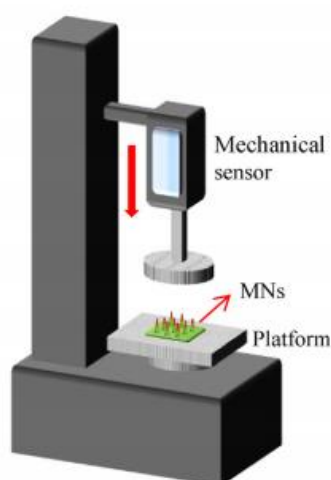


Figure 8 - Schematic representation of a texture analyser. Adapted from (Wang *et al.* 2018).

3.5. Permeation studies - Franz Diffusion Cells

3.5.1. Pig ear skin preparation

Fresh porcine ear skin was obtained at a local slaughterhouse preferably from healthy unmarked animals given that compromised skin can lead to false results (Dick and Scott 1992).

Initially, the skin was inspected to locate any possible lesion sites or visible capillary veins that would need to be dismissed for future studies. Next, the external part of the pig ear was separated from the underlying cartilage with the help of a scalpel, and any subcutaneous fat tissue was removed to better isolate the whole skin. The samples obtained were wrapped in aluminum foil and stored at -20°C until required.

For the permeation studies that follow, the full thickness membranes were allowed to thaw at room temperature for approximately 30 minutes before being cut into circles with a diameter equivalent to the donor compartment.

3.5.2. Permeation study

Whole skin permeation studies for both the model drug (calcein) and RV were performed using Franz Diffusion Cells (9 mm unjacketed Franz Diffusion Cell with 5 mL receptor, O-ring joint, clear glass, clamp, and stir-bar; PermeGear, Inc., USA). As a control for the study, empty MNs were also used as a condition for the permeation assay. The generic setup is represented in Figure 9.

Firstly, the receptor chamber was filled with 4.7 mL of PBS buffer pH 7.4, and a magnetic bar was added, allowing the system to reach 37°C on the magnetic stirring plate. MNs were placed in the center of the skin membrane and secured with medical adhesive tape. Then, pressure was applied with the index finger for a period of 10 seconds followed by the application of a 1.6 N force using the applicator (Micropoint Technologies, Singapore) for the same period of time. Both a calcein solution in PBS and hydrogels containing the drugs (calcein or RV) were used as controls. Exelon® patches were also used as a control for RV-loaded MNs study, applied on the skin according to the instructions. Following, the pig ear skin, with respective study condition, was mounted with the SC facing upwards, between the donor and receptor compartments, with a diffusion area of ~0.64 cm², and held in place with a metal clamp. To prevent evaporation, the donor chamber opening was sealed with Parafilm®. Using a micropipette coupled with a plastic straw, aliquots of 200 µL were collected from the receptor sampling port at set times of 3, 6, 8, and 24 hours, and the same amount of fresh preheated PBS medium was reintroduced into the receptor. Any air bubbles created were removed by carefully tilting the Franz Cells, letting the air escape through the sampling port. All the conditions were carried out, at least, in triplicate (n=3) under continuous stirring at 37°C for 24 hours and protected from sunlight exposure to prevent possible degradation of the compounds present. The skin used in the permeation studies for each condition, as well as the contents of the donor chamber, were collected and stored at -20°C, until needed for further studies.

Regarding the studies with the model drug, the control samples considered calcein dissolved in PBS (0.15 mg of drug per 150 µL PBS) and each hydrogel with calcein (0.15 mg per 150 mg of hydrogel), all in the same concentration as the MNs produced (0.1% w/w). For RV, the control samples were Exelon (0.5 cm² from an Exelon® patch 5 cm²) and each hydrogel with RV (0.9 mg per 150 mg of hydrogel).

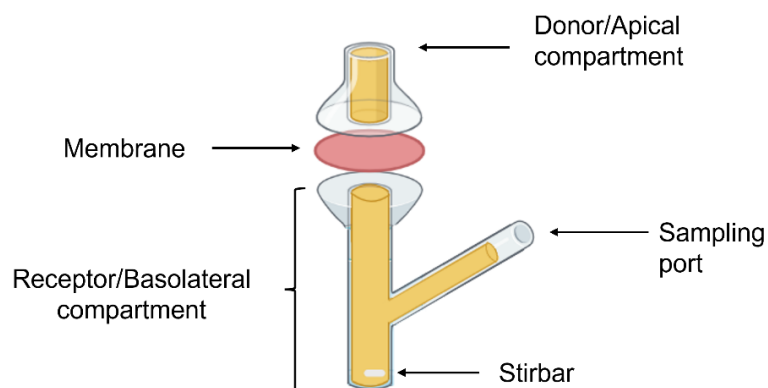


Figure 9 - Schematic representation of a Diffusion Franz Cell.

3.5.3. Quantification of drugs' permeation

With the aim of quantifying the calcein content in the basolateral compartment, a standard curve was prepared.

The stock solution was prepared by dissolving calcein in PBS buffer pH 7.4 with the help of a sonication bath (Sonica® Ultrasonic Cleaner), at a final concentration of 1.6 mM. The standards were obtained by dilution from the stock at concentrations of 12.5, 6.25, 3.13, and 1.56 μM in PBS.

Fluorescence intensity of the solutions was measured in a microplate reader (Synergy™ HT Multi-Detection Microplate Reader, Cytation®) with excitation and emission wavelengths of 485 nm and 528 nm, respectively (50%, top), and a linear standard curve was plotted. Three independent stock solutions, that resulted in three independent standard curves, were prepared (n=3).

Using the calibration curve, calcein concentration was calculated considering the fluorescence in each aliquot retrieved from the permeation study. Mass of calcein per 4.7 mL of PBS was obtained using Equation 1:

$$C_c = \frac{m_c}{V_t} \quad (1)$$

where C_c represents the calcein concentration in the acceptor chamber (mg/mL), m_c the mass of calcein (mg) and V_t the PBS volume in the acceptor chamber (4.7 mL).

The masses obtained were used to evaluate mathematically the apparent permeability coefficient (P_{app}) and the % of permeation (% P) using the formulas, respectively:

$$P_{app}(cm/s) = \frac{\sum m_a}{A \cdot m_0 \cdot t} \quad (2)$$

$$\% P = \frac{\sum m_a}{m_0} \times 100 \quad (3)$$

where $\sum m_a$ represents the sum of the drug mass permeating over time in the acceptor chamber (g), A is the area of diffusion in the Franz Diffusion Cell system (0.64 cm²), m_0 is the initial donor mass (g) and t the time (seconds).

For RV quantification, high-performance liquid chromatography (HPLC) analysis was conducted. Analysis was performed using a reversed-phase monolithic column (Chromolith®RP-18e, 100mm × 4.6mm i.d., Merck), connected to a Jasco (Easton, USA) HPLC system (pump PU-4180, autosampler AS-4050 and LC-Net II/ADC controller) coupled to a PDA detector (Jasco MD-4010, Start Wavelength = 200nm, End Wavelength = 400nm). The data processing was performed by ChromNAV2.0 HPLC software (Easton, USA). The UV chromatogram was acquired at 214 nm and the retention time of RV stood between 4.2 - 4.4 min. The mobile phase, degassed for 1 hour in an ultrasonic bath before use, consisted of PBS and acetonitrile (70:30, v/v) with pH adjusted with HCl to 4. The flow rate of the system was 1 mL/min.

For the quantification of drugs' permeation, skin permeation medium was used. It was obtained by the exposure of a circle of skin to the basolateral solution, overnight, in the same conditions as the permeation assays (37°C, under stirring). The apical compartment consisted only of water.

The stock solution of 1 mg/mL of RV in PBS 7.4, was diluted in skin permeation medium to obtain 5 standard concentrations ranging from 0.2 to 0.01 mg/mL (0.2, 0.1, 0.05, 0.02, 0.01 mg/mL). All samples investigated had the pH adjusted to 4 (JENWAY 550 pH meter (UK)).

The same calculation method mentioned above for the model drug was used for RV (Equations 2 and 3).

3.5.4. Quantification of the drug remaining in the apical compartment

The amount of compound remaining on the skin surface was carefully removed at the end of the skin permeation studies (after 24 hours) and stored at - 20°C until used.

For the model drug, 30 mg of each condition in the study was dissolved in 200 µL of PBS pH 7.4 and vortexed for 2 minutes. Next, samples were left for 30 minutes in a sonication bath followed by centrifugation at 10000 rpm at 20°C for, at least, 15 minutes (Allegra X-15R, Beckman Coulter). The visible pellet formation was discarded, and the supernatant was recovered and analyzed by fluorescence spectroscopy as described in section 3.5.3. For some instances, the extraction process was repeated a second time since the pellet still had a yellowish color which presupposes the presence of calcein in the system.

Regarding calcein, the mass of drug present was determined by interpolation of the calibration curve previously established. Given the mass of drug in the apical and basolateral, the percentage of drug retained in the skin was estimated using the mathematical formula:

$$\% \text{ Retained drug} = 100 - (\% \text{ of remaining drug in the apical} - \% P) \quad (4)$$

where % of remaining drug in the apical represents the percentage of calcein in the apical at 24 hours and % P the percentage of drug in the basolateral at 24 hours.

The extraction process remained the same for RV, differing only on the analysis method and the solvent and the volume used, in this case, the mobile phase (350 μ L). Quantification of the drug was obtained by HPLC analysis, which was performed under the conditions mentioned in section 3.5.3.

3.5.5. Skin digestion

After disassembling the Franz Diffusion Cell system, porcine skin was wrapped in aluminum foil, labeled, and stored at -20°C .

To determine the mass of drug retained in the full-thickness skin, RV samples were stripped of excess tissue, leaving only the diffusion of the skin area (0.64 cm^2) for analysis. Following this, the skin was placed in a 50 mL falcon and approximately 5 mL of mobile phase was added, enough for the ultraturrax device (Ultra-turrax, Janke & Kunkel IKA-Labortechnik, ULTRA-TURRAX T25) to be able to digest the skin at 12000 rpm for 2 min, or until the skin sample was completely destroyed. Each sample was then placed in a sonication bath for 30 minutes and immediately centrifuged at 4750 rpm for 20 minutes (Allegra X-15R, Beckman Coulter). The supernatant was collected and left to evaporate in a rotary evaporator (Rotary evaporator, Buchi, R200) using a stream of argon and a thermostatic bath at 40°C until the sample is fully dry and a white cast is formed in the glass tube walls.

Samples were resuspended in 500 μ L of mobile phase and centrifuged at 10000 rpm for 15 min. Some samples required a second centrifugation step. HPLC analysis was carried out in the same conditions as mentioned in 3.5.3.

3.5.6. Histology of the pig skin

Calcein skin samples resulting from the permeation assays were fixed with formaldehyde and sent to the histological service (ICBAS), where they were processed. Briefly, tissue was paraffin-embedded and sectioned at a thickness of 5 μm . Then, haematoxylin and eosin staining (H&E) samples histological analysis was performed by optical microscopy (Inverted Optical Microscope, Olympus, CK2), equipped with a digital camera (MotiCam S12). A total of 9 samples were analyzed, these being the 7 experimental permeation trial conditions, one skin sample from a permeation trial in which the donor compartment contained only water, and a skin sample where an MN was inserted into the skin for 10 minutes and posteriorly removed and analyzed.

To further investigate pore-forming structures in the skin, samples without staining were analyzed using fluorescence confocal microscopy. Images were recorded on a Leica Stellaris 8 confocal microscope (LeicaMicrosystems, Wetzlar, Germany) equipped with the Leica Application Suite X package (LAS X). Images were acquired with a resolution of 1024×1024 using a 10X/0.4 objective and then processed under ImageJ software (Fiji app, ImageJ2 version, freely available at <http://imagej.net/>).

3.5.7. Statistical analysis

Statistical analysis was performed using GraphPad Prism Software (Version 7 for Windows; GraphPad Software Inc, San Diego, CA, USA). The two-way ANOVA analysis of variance was used to assess the differences between formulations at all timepoints for the % permeation. One-way ANOVA analysis of variance was used to assess the differences between formulations at each timepoint of Apparent Permeability, % retained in the skin, and % remaining apical. One-way ANOVA analysis was also considered for the texture analysis' results.

4. Results and Discussion

4.1. Microneedles: preparation and optimization process

4.1.1. Hydrogels' preparation

Hydrogels are a three-dimensional polymeric network enriched in water, composed of either natural or synthetic polymers. The group of natural polymers is composed of polysaccharides and polyesters. These polymers stand out from the synthetic formulations due to their easy acquisition, as they derive from a renewable source, occurring naturally in nature or extracted from animals and plants. Also, natural polymers gain relevance for their inherent biocompatibility and bioactivity, in opposition to synthetic polymers, due to the resemblance with components present in the extracellular matrix (Aravamudhan *et al.* 2014).

In this study hydrogel-based MNs were produced with the intent to penetrate the skin and deliver the proposed drug. For hydrogel-based MNs preparation using PDMS templates, two characteristics were taken into account, the viscosity of the hydrogel, and the mechanical properties of the hydrogel in dry state. Hydrogels need to be easy to handle and able to penetrate the mould cavities of the template. On the other hand, adequate post-gelling stiffness was required for the MNs to pierce the skin without breaking.

From Figure 10 it can be noted that comparing the different formulations produced, alginate 7% (w/w) appears to be a more viscous hydrogel, while k-CRG 1% (w/w) appears to be the least viscous. The mixture of the two hydrogels seems to be somewhere in middle. In the end, 3 formulations with visible different physical properties were obtained. All formulations were used for MN production, during the optimization process.



Figure 10 - Viscosity comparison between three different hydrogel formulations. Formulations were placed in a Petri dish, then the dish was tilted 90° and the hydrogel run was observed for 15 seconds. In the left is alginate 7% (w/w), in the middle k-CRG 1% (w/w) and in the right alginate + k-CRG (1:1) (w/w).

As mentioned in the introduction, the model drug used in this study was calcein, a fluorescent compound. At first, a 1% (w/w) concentration of calcein was used however, as can be seen in Figure 11, the amount of calcein added was not able to be dissolved. Given that, the percentage of calcein incorporated in each hydrogel solution was reduced to 0.1% (w/w).

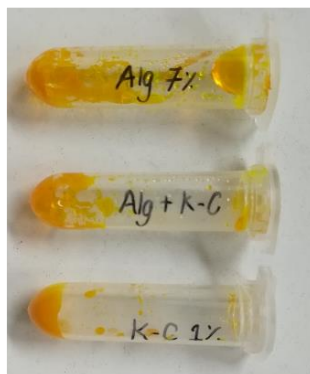


Figure 11 - Visual aspect of 1% (w/w) calcein in alginate 7% (w/w) (up), alginate + k-CRG 1:1 (w/w) (middle) and k-CRG 1% (w/w) (bottom).

4.1.2. Microneedle's fabrications - optimization process

Optimizing the MN fabrication process will allow the production of MN arrays in an efficient and reproducible manner.





The different methods of MN production are represented chronologically in the table below (Table 2). Initially, the production of MNs was based on the work developed by Chen *et al.*, 2012. Here, the MN molds were filled with hydrogel and horizontally centrifuged to ensure even distribution of the gel, to eliminate any air bubbles, and to allow the hydrogel to enter the mould cavities. However, using this approach, significant polymer loss was noticed, suggesting the amount of polymer added to each template was exceeding that supported by the molds used in the present study. In addition, the centrifugation cycles, besides being time-consuming, required high mechanical effort from the equipment. Therefore, all these factors were adjusted, resulting in method 2. Nevertheless, polymer loss was still an issue in the centrifugated first-layer so, the quantity of polymer added in the first layer was reduced, as well as the addition of an extra incubation and centrifugation step. The result was MNs with no visible picks which suggest the importance of the high centrifugation cycles, mainly in the first layer.

Besides centrifugation, temperature represented an important factor for the success of MN production. In the centrifugation cycles, the temperature influenced the fluidity of the hydrogel, and thus, the pore-filling capacity. This might suggest the importance of temperature during the production of the devices. In the literature, no articles were found that mentioned the influence of this factor on the production of MNs. Most often the temperature used when producing the devices is not mentioned (Dathathri *et al.* 2019; González-Vázquez *et al.* 2017; Sabri *et al.* 2020).

Regarding the drying process, it contributed to faster water removal from the system which meant it needed to be done in a controlled manner.

The optimized process, method 4, resulted from the conclusions mentioned above. This process was used in the production of all MNs under study in this work - drug-free, calcein, and RV-loaded MNs.

Table 2 - Summary of MN production methods optimization. The different color represents the number of layers added to each mold.

		Method 1	Method 2	Method 3	Method 4
Number of layers					
Time		3 days	3 days	3 days	3 days
Conditions per day	Day 1	50 mg; 3500 rpm; 30°C; 1 hour	100 mg; 2500 rpm; 30°C; 30 minutes	50 mg; 500 rpm; 15°C; 15 minutes	25+25 mg; 3500 rpm; 30°C; 1 hour
	Day 2	150 mg; 3500 rpm; 30°C; 1 hour	50 mg; 500 rpm; 15°C; 15 minutes	100 mg; 500 rpm; 15°C; 15 minutes	50 mg; 3500 rpm; 30°C; 1 hour
	Day 3	incubation; 100 rpm; 25°C; 3 hours	incubation; 150 rpm; 25°C; 3 hours	incubation; 150 to 250 rpm; 25°C; 2 hours centrifuged; 500 rpm; 10°C; 1 hour incubated; 150 rpm; 25°C; 3 hours	50 mg; 3500 rpm; 30°C; 1 hour incubation; 150 rpm; 25°C; 3 hours
Observations		Visible polymer loss. Possible overfilling of the micromold	Polymer loss detected after first-layer centrifugation	After detachment, no picks were visible	No significant losses. Needles visible to the naked eye

4.2. Calcein-loaded microneedles

4.2.1. Calibration curve

The graph represented in Figure 12 establishes the relationship between the concentration of calcein in solution and its fluorescence intensity. The resulting calibration curve is a weighted average of 3 concordant and independent curves (n=3) of 5 different standard solutions. Data were fitted to a linear regression analysis, where the coefficient of determination (R^2) proximity to 1 attests to the linearity of the system. (Moosavi and Ghassabian 2018)

All samples generated from the permeation studies were intercepted on the calibration curve, Fluorescence intensity (a.u.) = 4×10^{-6} [calcein] + 2.63×10^3 , in order to obtain the concentration of calcein ($\mu\text{g/mL}$).

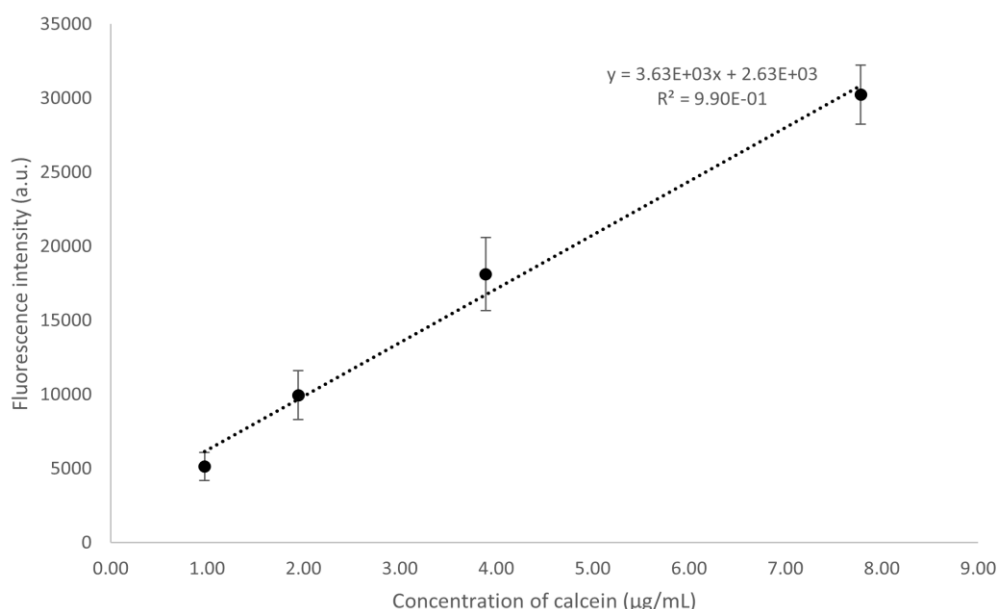


Figure 12 - Calibration curve for calcein (data represents median \pm standard deviation, n=3).

4.2.2. Morphology analysis

With the aim of assessing the morphology of each MN type made from different formulations, SEM analysis was first carried out for drug-free MNs. Figure 13 shows the results obtained for each hydrogel formulation with two different MN heights (400 and 800 μm). All samples developed were analyzed in duplicates.

Both alginate and alginate + k-CRG mixture MNs presented a three-dimensional (3D) pyramidal structure with sharp tips. However, when comparing both formulations in the

different sizes, 800 μm arrays (Figure 13B and 13D) presented MNs with a more pronounced curvature, especially in the first row. These shortcomings, marked in red, can be caused either by the height of the MNs, since the bigger the structure the less stable it might become over time, or by the detachment process itself. After the drying process, the arrays are separated from the micromould using duct tape to grab onto the MN system and pulling the MNs from one corner to the other, possibly causing the curvature observed in the first rows of MNs. Contrarily, k-CRG hydrogel, despite being able to penetrate the pores of the mold, viewed by Figures 13E and 13F, was not able to preserve the MN pyramidal structure for neither of the MN heights. Figures 13E and 13F portray the failure in the MNs structure. Therefore, k-CRG MNs were discarded from further studies given the absence of the necessary characteristics to puncture the skin.

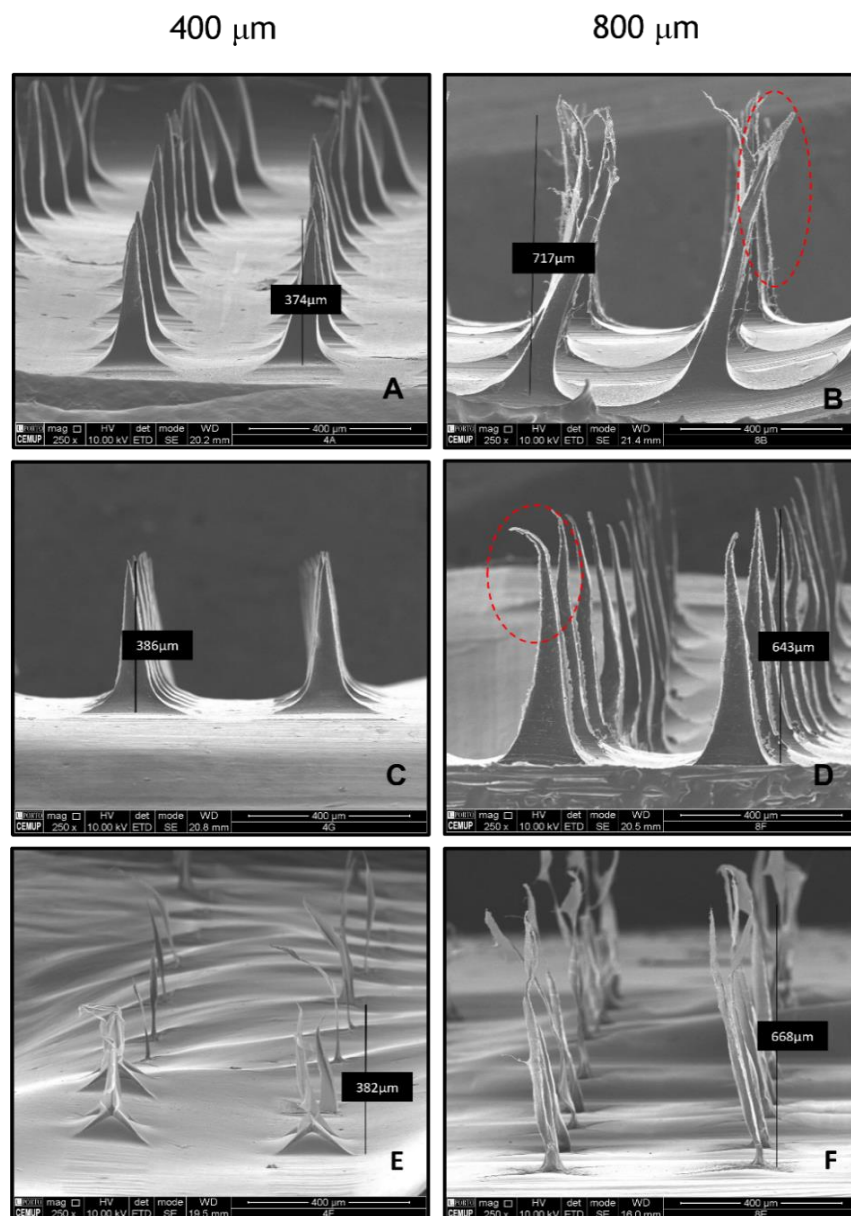


Figure 13 - Representative SEM images of drug-free microneedles with two needle sizes. (A) and (B) MN Alginate 7%; (C) and (D) MN Alginate 7% + k-CRG 1%; (E) and (F) MN k-CRG 1%.

After the elimination of one of the experimental formulations (k-CRG 1% (w/w)), MN arrays were produced by the incorporation of the model drug, calcein, into each hydrogel. This time only two formulations were used for both MN sizes. The purpose of this study is to evaluate the effect of the model drug in the MN arrays' morphology.

As found in drug-free MNs, the curvature of the structure can also be observed for drug-loaded MNs, which appear to be more visible in the 800 μm alginate + k-CRG condition - Figure 14D. In this case, since the curvature is the same in all the MNs, the cause may be associated with manipulation of the needles during detachment or by the weight of the structure. In opposition, 400 μm alginate MN only experienced this curvature in the first row of MNs. Although some defects in the 3D structure of these devices are perceptible, in general, they appear to be suitable for permeation studies.

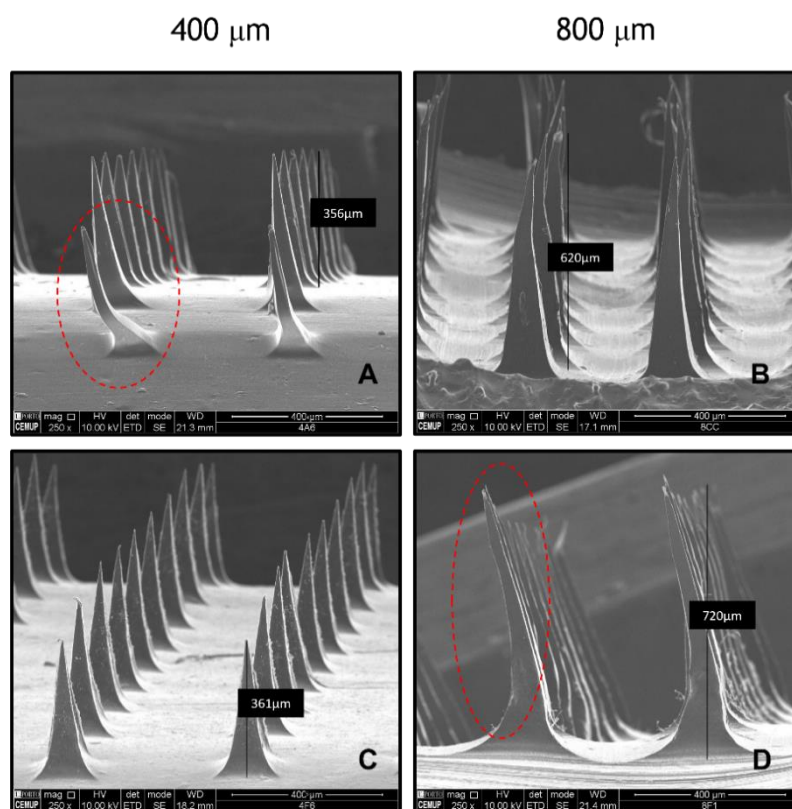


Figure 14 - Representative SEM images of calcein-loaded microneedles with two needle sizes. (A) and (B) MN Alginate 7%; (C) and (D) MN Alginate 7% + k-CRG 1%.

When processing the samples, the height of the MNs, from the center of the pyramid's base to the vertex, was measured. Figures 13 and 14 demonstrate a lower height for all MNs compared to the expected size conferred by the mould. According to the manufacturer, MN molds enable the production of 10 x 10 arrays with a pyramid base established between 150 or 200 μm and a height of 400 or 800 μm . Neither of the conditions produced MNs with the exact height set up by the moulds, nevertheless, 400 μm moulds produced microneedles with heights more similar to the moulds, ranging from 356 to 386 μm as it can be seen by the above figures. Conversely, 800 μm MNs present a lower height of around 700 μm , compared to the 800 μm expected. The shrinkage of the MNs can be explained by the loss of water experienced when the hydrogel present in the moulds is

exposed to the drying process, or by the capacity of the hydrogels to travel through the pore moulds and form the MN tips. However, it cannot be discarded the possibility that the height of the MNs that the manufacturer states is relative to the height of the MNs considering the mould base, and if this approach was chosen, the height would certainly be more similar to the expected, based on the characteristics of the mould. Nevertheless, considering only the size of the MNs, drug delivery by this factor is not compromised since passage through the SC only requires an MN length of 10-20 μm in humans (Makvandi et al. 2021). Both MN sizes allow the delivery, in a first instance, to the dermis (Prausnitz and Langer 2008), which is in accordance with the goal of systemic delivery of the therapeutic drug.

Throughout this analysis, it was considered that a percentage of defects equal to or less than 10% (10 in 100 needles) constituted MNs with suitable structure for the study.

4.2.3. Texture analysis

For a MN to penetrate the skin effectively and deliver the therapeutic drug, the force that is applied must not exceed its fracture force, i.e., the array should not deform or break when transdermally applied. In this study, the compression force was investigated. The profiles of force (F) versus displacement after an axial force load are represented in Figure 15. A general idea of which type of MN offers the best resistance to force can be drawn by analyzing these profiles.

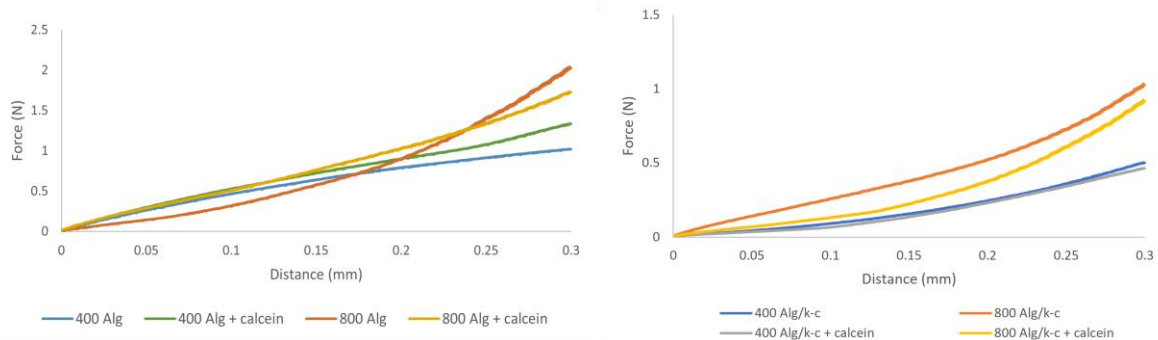


Figure 15 - Representative force-displacement curves of drug-free (left) and calcein-loaded MNs (right).

Table 3 allows some conclusions to be drawn about the influence of the presence of calcein, as well as the impact of the type of hydrogel and the height of the MN on the compression force. The force measured by the probe corresponds to approximately 2 MNs per reading which requires the values to be divided in half in order to take the fracture force reading for one MN per array. The reading of a reduced set of needles by the probe, as opposed to the overall array at once, acknowledges the heterogeneity factor of the device, since not all MNs break at the same time (Sabri *et al.* 2020).

For the production of a robust MN array, capable of piercing the skin, the failure force per needle needs to exceed the force required to successfully insert the MN into the skin.

Yu *et al.* 2017 produced a patch containing MNs produced with alginate and hyaluronate and reported that the MNs produced were able to surpass the SC since the fracture force experienced by the needles produced in the study was inferior to 0.098N/needle (Yu *et al.* 2017). Additionally, Donnelley *et al.* have suggested that an insertion force as low as 0.03 N/needle may be enough to pierce the SC (Donnelley *et al.* 2013). Taking this into account, in theory, all MNs in this study are able to be inserted into the skin.

Table 3 - Profile of the compression forces of different MNs.

	Force (N)		Force/needle
MN 400 μ m Ag	1.02 \pm 0.20	£	0.51
MN 800 μ m Ag	2.02 \pm 0.29	****	1.01
MN 400 μ m Ag + calcein	1.30 \pm 0.25	#	0.65
MN 800 μ m Ag + calcein	1.65 \pm 0.32	***, ###	0.83
MN 400 μ m Ag_k-CRG	0.52 \pm 0.12	£	0.26
MN 800 μ m Ag_k-CRG	0.98 \pm 0.22	****	0.49
MN 400 μ m Ag_k-CRG + calcein	0.45 \pm 0.07	£	0.23
MN 800 μ m Ag_k-CRG + calcein	0.92 \pm 0.16	****	0.46

Data represented is a mean and SD of all values measured. *** P < 0.001 for MN 800 calcein (Alginate) Ag vs MN 400 calcein Ag; **** P < 0.0001 for MN 800 calcein Ag_k-CRG vs MN 400 calcein Ag_k-CRG; **** P < 0.0001 for MN 800 Ag vs MN 400 Ag; **** P < 0.0001 for MN 800 Ag_k-CRG vs MN 400 Ag_k-CRG; # P < 0.05 for MN 400 calcein Ag vs MN 400 Ag; ### P < 0.001 for MN 800 calcein Ag vs MN 800 Ag. £ represent P > 0.05, i.e., no statistical significance.

To analyze the differences present among the values presented in Table 3, a statistical significance study was created. Concerning the presence of a drug, calcein has seemingly increased the compression force for 400 μ m alginate MNs, contrary to what happens with 400 and 800 μ m alginate + k-CRG MNs that don't present a significant difference compared to the respective drug-free MNs. As for 800 μ m alginate calcein loaded-MNs, there is a decrease in compression force when compared to their respective drug-free array. As for height, the results show that drug-free MNs and calcein-loaded MNs have a compression force superior for 800 μ m MNs compared to 400 μ m MNs, as shown in Table 3.

This study is based on hydrogel MNs, namely alginate and k-CRG, agents competent for the retention of water molecules in the system (Qureshi *et al.* 2019; Tønnesen and Karlsen 2002). As the percentage of water retained influences the compression force, and the drying process is not strictly controlled, variations in the measurements were to be expected (as pointed out by the standard deviation (SD) values).

In general, it is visible that alginate MNs exhibit compressive forces superior to those experienced by MNs of the mixture over all conditions.

4.2.4. Permeation assay

To characterize the release profile of the MN devices, the permeation of the model drug was studied. Alginate and alginate + k-CRG MNs were inserted into porcine skin and subsequently, the drug release was monitored for 24 hours (Figure 16). For comparison, a calcein PBS solution and both hydrogel formulations, containing the same amount of drug as the MNs, were used as controls. The measurements of drug release were performed cumulatively.

As shown in Figure 16, skin permeation of calcein increases over time, reaching a maximum percentage of permeation of approximately 40% after 24 hours, for all conditions. At 3 hours no significant permeation is observed for any condition. However, at 6 and 8 hours, alginate MNs potentiate a higher % of permeation than alginate + k-CRG MNs, being 800 μm alginate MNs the ones with a higher percentage. In this interval of time is apparent that alginate MNs have superior calcein release than its hydrogel, while alginate + k-CRG MNs have lower drug release compared to the corresponding hydrogel.

Regarding MN height, 800 μm MNs seem to potentiate a faster release of the model drug over time ($P > 0.05$), contrary to what happens to 400 μm MNs. The fact that there are differences between hydrogel *versus* MN demonstrates that these devices when implemented, induce some changes in the system. In this case, alginate MNs are shown to have faster release over time, whereas the mixture reduced the experienced % of permeation when compared to the respective hydrogel.

Despite the lack of statistical significance between the calcein-loaded MNs of different needles' sizes, and having in mind a systemic application for RV, 400 μm MNs were discarded from this work, as they are expected to be more suitable for topical applications given the quicker release time (Ito *et al.* 2013). Thus, both formulations of MNs with 800 μm of tip length proceed to further studies.

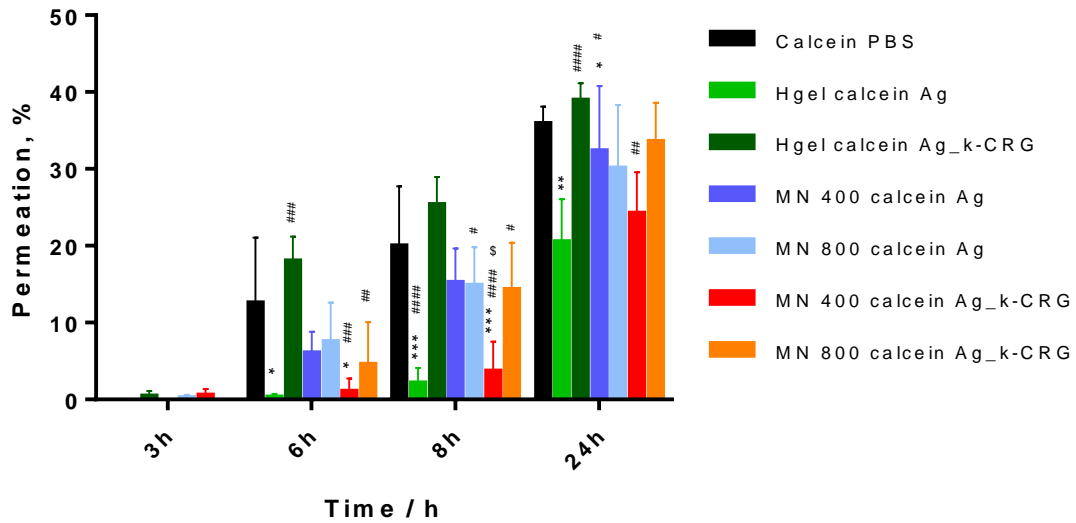


Figure 16 - Percentage of permeation of calcein for porcine skin treated with free calcein, calcein-loaded hydrogels, and calcein-loaded MNs of two different heights, at different timepoints. * P < 0.05 for Ag calcein hydrogel formulation and MN 400 calcein Ag_k-CRG vs free calcein at 6 hours; * P < 0.05 for MN 400 calcein Ag vs free calcein at 24 hours; ** P < 0.01 for Ag calcein hydrogel formulation vs free calcein at 24 hours; *** P < 0.001 for Ag calcein hydrogel formulation vs free calcein at 8 hours; *** P < 0.001 for MN 400 calcein Ag_k-CRG vs free calcein at 8 hours; # P < 0.05 for MN 800 calcein Ag and MN 800 Calcein Ag_k-CRG vs hydrogel formulation at 8 hours; # P < 0.05 for MN 400 calcein Ag vs hydrogel formulation at 24 hours; ## P < 0.01 for MN 800 calcein Ag_k-CRG vs hydrogel formulations at 24 hours; ### P < 0.001 for Ag_k-CRG calcein hydrogel formulation and for MN 400 calcein Ag_k-CRG vs hydrogel formulations at 6 hours; #### P < 0.0001 for Ag calcein hydrogel formulation and MN 400 calcein Ag_k-CRG vs hydrogel formulations at 8 hours; ##### P < 0.0001 for Ag_k-CRG calcein hydrogel formulation vs hydrogel formulation at 24 hours; \$ P < 0.05 for MN 400 calcein Ag_k-CRG vs 400 calcein Ag_k-CRG at 8 hours; Statistical significance was only represented for MN formulations vs free calcein solution or vs calcein-loaded hydrogels. The bars/points represent the mean ± SD of the permeability for three independent experiments (n=3).

All conclusions are in agreement with the values obtained in the apparent permeability (P_{app}) calculations (Figure 17). Shakel and co-workers also reported the study of calcein permeation using pig ear skin as one of the model drugs. Although the permeation results are only available for the first 3 hours, the P_{app} order of magnitude when compared with the results obtained in this study, is the same, i.e., 10^{-6} cm/sec (Shakel *et al.* 2019). Despite the variability associated with the permeation study using this full-thickness membrane, the results obtained are comparable.

Even though approximately 40% of calcein was able to cross the skin barrier, visible in all conditions, the remaining 60% were either retained in the skin or remained in the apical compartment of the Franz Diffusion Cells.

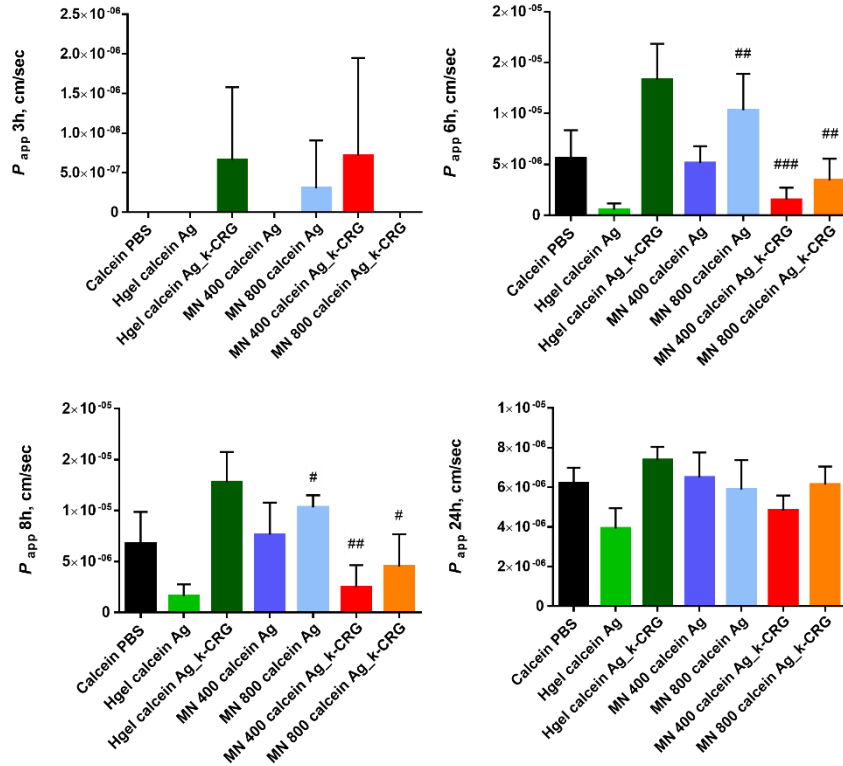


Figure 17 - Apparent permeability coefficient for 3, 6, 8, and 24 hours of calcein for porcine ear skin treated with free calcein, calcein-loaded hydrogels, and calcein-loaded MNs of two different heights. # $P < 0.05$ for MN 800 calcein Ag vs hydrogel formulations at 8 hours; # $P < 0.05$ for MN 800 calcein Ag_k-CRG vs hydrogel formulations at 8 hours; ## $P < 0.01$ for MN 800 calcein Ag and MN 800 Ag_k-CRG vs hydrogel formulations at 6 hours; ### $P < 0.001$ for MN 400 calcein Ag_k-CRG vs hydrogel formulation at 8 hours; # $P < 0.05$ for MN 800 calcein Ag vs hydrogel formulations at 8 hours; # $P < 0.05$ for MN 800 calcein Ag_k-CRG vs hydrogel formulations at 8 hours; ## $P < 0.01$ for MN 800 calcein Ag and MN 800 Ag_k-CRG vs hydrogel formulations at 6 hours; ### $P < 0.001$ for MN 400 calcein Ag_k-CRG vs hydrogel formulation at 8 hours; Statistical significance was only represented for MN formulations vs free calcein solution or vs calcein-loaded hydrogels.

Figure 18 shows the overall scenario of calcein distribution in the permeation assay system. Just as a similar permeation profile at 24 hours was found for all conditions under study, the same is true for the remaining system, conclusions drawn from Figure 18. Calcein was mainly retained in the membrane with percentages reaching 60%, while a small percentage was found in the donor chamber ($\pm 10\%$). It should be noted that the retention percentage values are only estimated (arithmetic value) since no skin destruction for further drug quantification assay was performed on the pig ear skin after 24 hours.

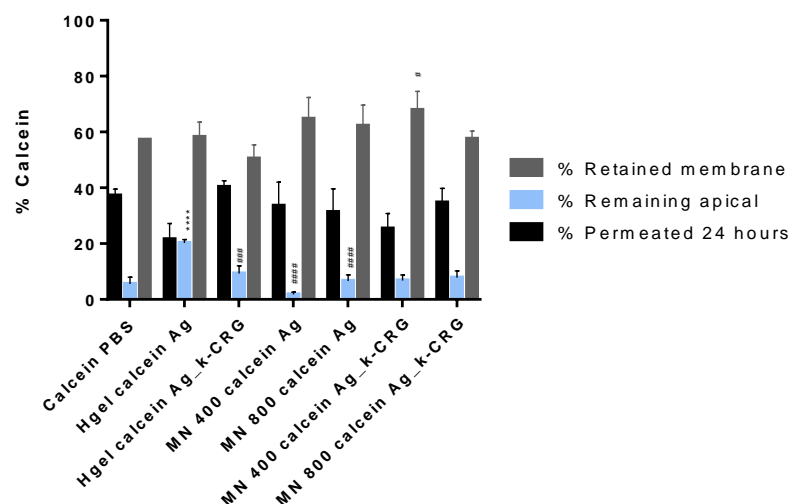


Figure 18 - Distribution of calcein among permeated, retained, and non-permeated through the porcine skin after 24 hours. The bars/points represent the mean \pm SD of the permeability for at least three independent experiments ($n = 3$). **** $P < 0.0001$ for Ag hydrogel formulation vs free calcein remaining in the apical; ### $P < 0.001$ for Ag_k-CRG hydrogel formulation vs hydrogel formulation remaining in the apical; #### $P < 0.0001$ for MN 400 Ag and MN 800 Ag vs hydrogel formulation remaining in the apical; # $P < 0.05$ for MN 400 Ag_k-CRG vs hydrogel formulation retained in the membrane. Permeation statistical analysis can be seen in Figure 16.

4.2.5. Optical and fluorescence confocal microscopy analysis

After being prepared, the skin samples were observed using optical microscopy and fluorescence confocal microscopy. In the second study, the presence of the dye interfered with the reading of the samples containing calcein so, in this case, the samples were observed without H&E staining.

Optical microscopy analysis was performed for nine conditions. All samples are displayed with the epidermis oriented to the right as indicated by the symbol # in Figure 19A. After a prolonged exposure of the pig ear skin to water, Figure 19A, the skin structure is hydrated. Compared to the skin sample not exposed to the permeation assay, Figure 19E, the skin thickness of the sample subjected for 24 hours to water increased from 1207 μm to 2389 μm . The conclusions drawn by Dąbrowska and colleagues with regards to the morphologic modifications in human skin after hydration are in concordance with the visible alterations shown in Figure 19A, which presents a smoother skin surface and an increase in skin thickness (Dąbrowska *et al.* 2016).

Regarding the calcein PBS sample, a “lacy” structure is visible in Figure 19B. In red is marked the transition site between a skin area that was in prolonged contact with the calcein solution and an area that had no contact with the solution. The apparent degradation of the skin structure visible in Figure 19B is not unique to this condition. Although more pronounced here, it is likewise present for the samples containing both types of hydrogel formulations, being more prominent for the hydrogel mixture (Figure 19D). This indicates that the penetration made by calcein under these conditions may be affected by this phenomenon.

In contrast to all other conditions, Figure 19E concerns a skin sample not subjected to a permeation assay. Having been in contact with a MN array for 10 minutes, the darker pink areas may indicate the presence of a needle, or, on the other hand, folds caused by the handling of the sample when mounting it on the slide. While the structure marked with an (*) appears to be an artifact caused by manipulation of the sample, the structures marked with an arrow could be the responsibility of the MN array. Given the short period of time that the system was inserted into the skin, possible needle marks are more difficult to observe. Consequently, the remaining conditions represent an interval of exposure of 24 hours.

Figure 19D is the result of skin contact with alginate, however, the full thickness membrane shows some folds that could be mistaken for skin breakdown caused by MNs, marked with (*). This proves the presence of alterations in the skin morphology caused by skin manipulation.

Figure 19F through I portray skin samples subjected to different MN arrays. All the MN skin samples present a darker structure resembling the presence of an MN that punctured the skin. The lengths of the structures are shown below and appear to be superior to the actual size of a MN height stated in section 4.2.2.

The site where an MN has been inserted can be identified by the triangular shape left on the skin surface due to the MN base, as well as the change in coloration of the area (darker pink). However, the measurement of this structure may not be faithful to the pore created by the MN as the skin may experience some folds or breaks during the processing of the skin for analysis. Furthermore, the darker area of the skin may indicate the presence of the MN but also the diffusion of the model drug used in the study, causing difficulty in understanding between the end of a pore caused by the MN and the beginning of an artifact caused by manipulation or diffusion of the compound. Therefore, the measurement of the puncture structures does not allow conclusions to be taken as to the height of the MN used.

The inconsistent distribution of the skin puncture structures caused by MNs in some of the preparations is also observed by this analysis.

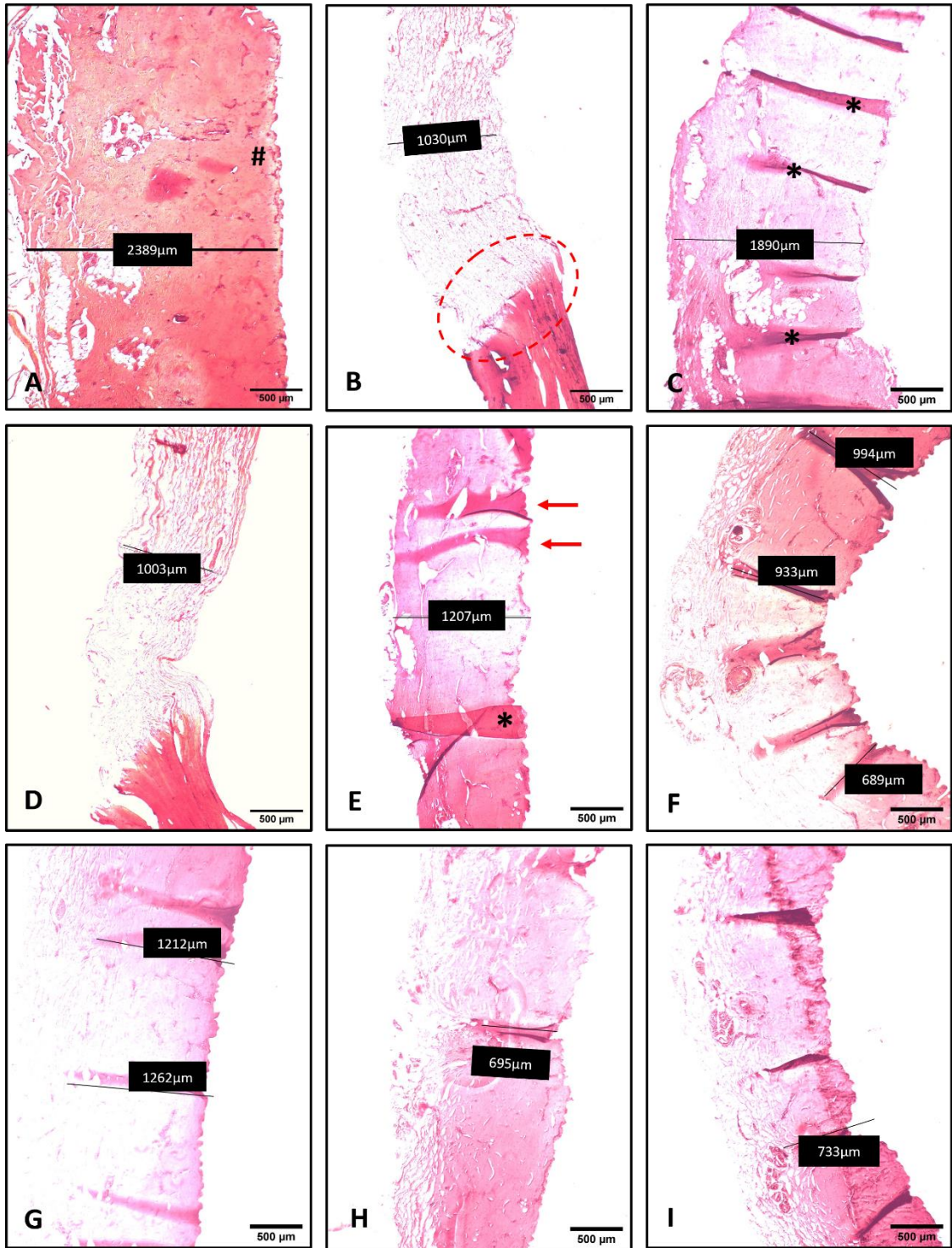


Figure 19 - Optical microscopy analysis of all conditions in study (H&E coloration) of the skin samples resultant from the permeation assay. Skin treated with A- water for 24 hours; B- calcein PBS; C- calcein-loaded alginate hydrogel; D- calcein-loaded alginate + k-CRG hydrogel; F- 400 MN calcein-loaded alginate; G- 800 MN calcein-loaded alginate; H- 400 MN calcein-loaded alginate + k-CRG; I- 800 MN calcein-loaded alginate + k-CRG. Sample E corresponds to pig ear skin treated with a 800 MN calcein-loaded alginate + k-CRG for 10 minutes. The # symbol represents the orientation of the SC. Red arrow indicates the structures possibly created by the MNs. The symbol * represents the folds in the skin.

Results from fluorescent confocal microscopy can be seen in Figure 20. All samples presented in Figure 20 maintain the same orientation established above. Figure 20A shows the morphology of pig ear skin using water as the component in the apical chamber, for 24 hours. Punctually, for this sample, the fluorescence microscopy observation was performed with the sample stained with H&E, which gives it the pink coloration shown, since it was not marked with calcein, contrary to the remaining conditions. Additionally, due to the high thickness of the sample, two images of the same condition in the same magnification were taken to be able to observe the skin in its entirety. Here the thickness of the skin appears to be increased possibly due to the large hydration of the structure. As the skin can do the uptake and retention of water it is plausible to assume that morphological changes may occur. Dąbrowska *et al.* 2016 studied the influence of water exposure on human skin thickness and roughness and verified that the contact of skin with water for up to 60 minutes generates a smoother skin surface as well as an increase in thickness of the SC. The direct comparison with dry skin allowed to conclude that the increase in thickness only occurred in the SC, while the remaining skin layers stayed intact (Dąbrowska *et al.* 2016). These observations may explain the change in skin appearance namely skin thickness observed in Figure 20A.

Calcein PBS skin sample is represented in Figure 20B. A change in skin structure is visible when compared to Figure 20A. The skin has a "lacy" appearance, suggesting that decomposition of skin components has occurred, which would therefore increase skin permeability. This event was proven to be caused by contact with calcein because the surrounding skin (no contact with calcein solution) appears unchanged. Since there is degradation of the skin in the environment containing calcein PBS, the calcein signal is expected to be less intense once the majority of the compound permeated to the basolateral compartment.

Regarding calcein-loaded hydrogel formulations, alginate, and alginate + k-CRG hydrogels, skin samples are represented in Figures 20C and D, respectively. The "lacy" appearance of the skin reported for the calcein PBS sample is also visible in both these samples.

Figure 20E presents the morphology of the skin when in contact with a MN array for 10 minutes. Here an 800 μm alginate + k-CRG MN was inserted into the skin in the same manner as the MNs inserted for the permeation assay and remained in direct contact for a period of 10 minutes. After that time, the MN array was removed, and the skin sample was processed. On the surface, it is possible to observe, what appears to be, a disruption of the SC caused by the perforation of a MN.

As for the MN skin samples, they all appear to have invaginations on the skin surface, similar to the hydrogel samples.

The green coloration shown represents the intensity of the calcein signal on the ear pig skin. It is possible to observe that the signal is more intense in the 400 μm MNs when compared to the 800 μm MNs, confirming their potentiality for topical drug delivery due to higher skin retention of the model drug.

All samples containing MNs, Figures 20E to I, present some structures, marked by red arrows, that appear to be caused by the perforation of the MN into the skin. As expected by the different lengths in needle tip, the ruptures caused in the skin differ in size. However, the breaks do not appear to be linearly distributed. This can be explained by the mounting of the sample on the slides as the skin at this thickness (5 μm) has a malleable

structure. Putting this data into perspective, a sheet of A4 paper could be around 0.3 to 0.5 mm thick.

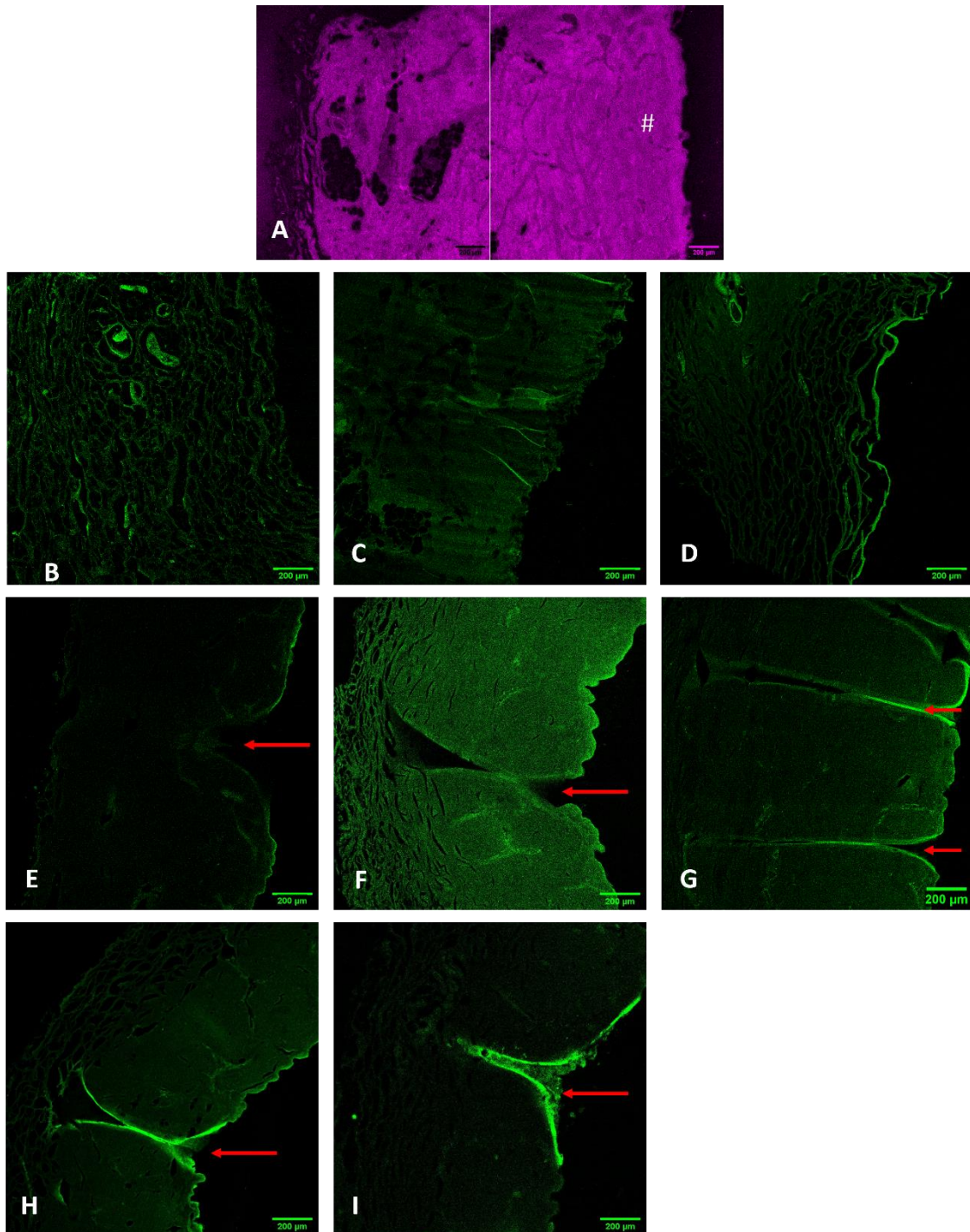


Figure 20 - Fluorescence confocal microscopy analysis of skin samples resultant from the permeation assay. Skin treated with A- water for 24 hours; B- calcein PBS; C- calcein-loaded alginate hydrogel; D- calcein-loaded alginate + k-CRG hydrogel; F- 400 MN calcein-loaded alginate; G- 800 MN calcein-loaded alginate; H- 400 MN calcein-loaded alginate + k-CRG; I- 800 MN calcein-loaded alginate + k-CRG. Sample E corresponds to pig ear skin treated with a 800 MN calcein-loaded alginate + k-CRG for 10 minutes. The # symbol represents the orientation of the SC. Red arrow indicates the structures possibly created by the MNs.

4.3. Rivastigmine-loaded microneedles

4.3.1. Calibration Curve

To analyze the results produced by the permeation assay of RV, a calibration curve was required. The relationship between the concentration of RV (mg/mL) and the area under the curve (AUC) determined in HPLC measurements was plotted, resulting in the linear regression curve shown in Figure 21.

The calibration curve presented was generated as the average of three independent curves (n=3) of 5 different standard solutions. The concentration values chosen are within the analytical limits of the samples. As previously described for calcein (section 4.2.1), the coefficient of determination (R^2) confirms the linearity of the system due to its proximity to 1.

All samples generated from the permeation studies were analyzed by HPLC. Areas retrieved were intercepted on the calibration curve, $AUC = 2.002 \times 10^7 [RV] - 1.371 \times 10^4$, in order to obtain the concentration of RV (mg/mL).

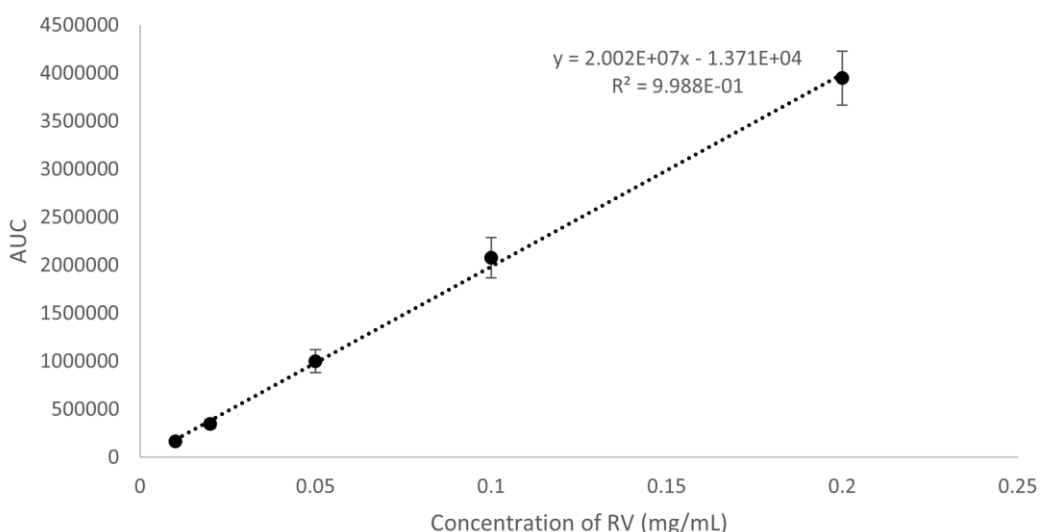


Figure 21 - Calibration curve for RV (data represents median \pm standard deviation, n=3).

4.3.2. Morphology analysis

Regarding RV-loaded MNs, the number of study conditions was reduced: it was possible to conclude that of the two sizes of MNs, and with the goal of drug delivery at the systemic level, 800 μ m MNs stood as the most promising. With that in mind, 800 μ m RV-loaded MNs were produced for both formulations and the morphological results can be seen in Figure 22.

Comparing alginate and alginate + k-CRG MNs, the two had in common the ability to maintain a 3D triangular pyramid shape. However, Figure 22A, corresponding to an RV-

loaded alginate MN device, showed a thinner and more tapered structure with curved tips, which can compromise the mechanical strength of the array, and therefore, the perforation of the skin. This phenomenon, not observed under the same conditions for calcein-loaded MNs (Figure 14B), suggests the alteration of the morphological behavior of MNs with the addition of this drug, even though calcein and RV have similar characteristics since these molecules both have hydrophilic characteristics and present low molecular weight (Oh *et al.* 2008; Sadowsky *et al.* 2010).

In this case, the mixture of the hydrogels condition - Figure 22B - presents a more satisfactory structure. Curiously, though a tilt in the base-working structure is observed in the MNs in all conditions, the permanence of this curvature belonged to the MNs produced with alginate alone in both drug-free and drug-loaded batches. However, in this case, as can be seen in Figure 22B, the base tilt is more pronounced for the alginate + k-CRG MN array. This phenomenon may be caused by the drying process, as the water loss from the hydrogel is not strictly controlled.

When directly comparing both RV-loaded MNs with their respective drug-free MN (Figure 13 B and D), the overall structure seems to not have been altered.

With regard to the height of the MNs, it can be seen that the values remain below those promised by the micromoulds producer.

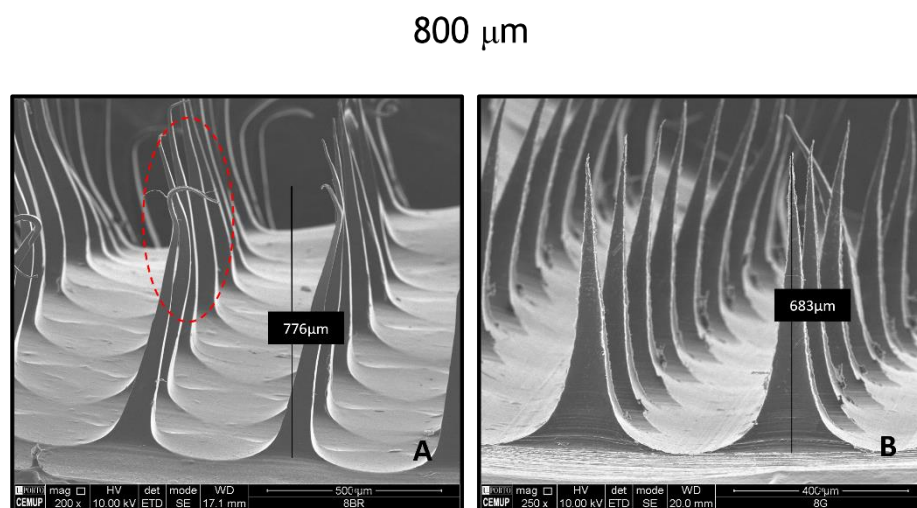


Figure 22 - Representative SEM images of RV-loaded microneedles. (A) MN Alginate 7%; (B) MN Alginate 7% + k-CRG 1%.

4.3.3. Texture analysis

As with the model drug used in this study, the mechanical properties of RV-loaded MNs were also investigated. Figure 23 represents the profile of force *versus* displacement after an axial force load inflicted onto the MNs.

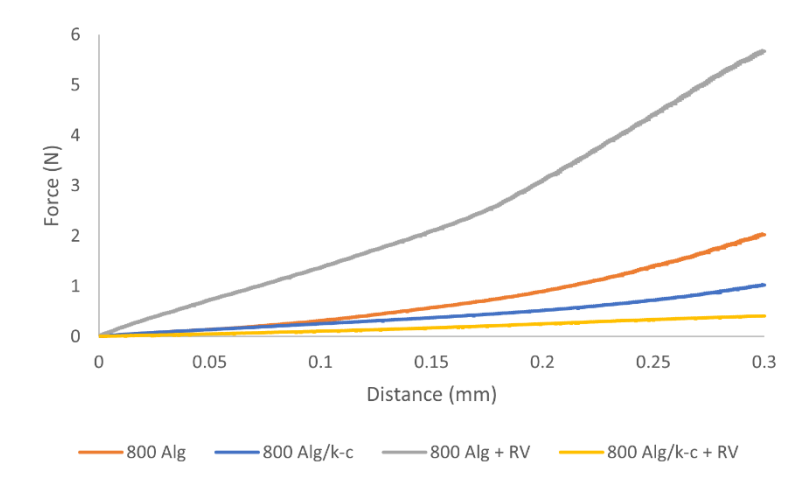


Figure 23 - Representative force vs displacement curves for 800 μm drug-free and RV-loaded MNs.

Table 4 shows the influence of RV on the mechanical strength of each type of hydrogel-derived MNs. From the compressive force values presented, it is possible to infer that there is an influence on the mechanical properties of the gel when RV is present.

On one hand, RV-loaded alginate MNs experience an increase in compressive strength by more than two times when compared to drug-free alginate MNs, reaching the 5.74 N of force per reading. By opposition, RV-loaded alginate + k-CRG MNs force is reduced by half, experiencing the same values seen in calcein-loaded MNs with 400 μm of height (section 4.2.3). Nevertheless, as stated for calcein MNs, RV MNs experience a compression force *per* needle superior to 0.098 N/needle which means the capacity to cross the SC is not lost (Yu *et al.* 2017).

While the mechanical properties of calcein-loaded MNs were only altered for calcein-loaded alginate MNs when compared to drug-free MNs, for RV-loaded MNs the influence was visible for both hydrogel formulations. Other works have shown that the loading of compounds into an MN system may alter the compression force experienced. Bhatnagar *et al.* 2018 developed a dissolving polymeric MN array based on polyvinyl alcohol and polyvinyl pyrrolidone for the delivery of an antibiotic, besifloxacin, through the cornea. The texture characterization, using axial and transverse force, showed a decrease in compression force of besifloxacin-loaded MNs of 7.64 N when compared to 8.80 N for drug-free MNs (Bhatnagar *et al.* 2018). Another study, based on the transdermal delivery of a compound normally applied intradermally, tetanus toxoid (TT), demonstrated the reduction of the maximum force for a displacement of 0.5 mm for TT-loaded MNs compared to blank MNs (Pattarabhiran *et al.* 2019).

In a direct comparison of the two hydrogel formulations, RV-loaded alginate MNs have approximately 10 times the compression force of alginate + k-CRG MNs.

Table 4 - Profile of the mechanical forces of drug-free and RV-loaded MNs.

	Force (N)		Force/needle
MN 800 μ m Ag	2.02 \pm 0.29	£	1.01
MN 800 μ m Ag + k-CRG	0.98 \pm 0.22	\$\$\$\$	0.49
MN 800 μ m Ag RV	5.74 \pm 0.89	****	2.87
MN 800 μ m Ag + k-CRG RV	0.45 \pm 0.09	*, #####	0.23

Data represented is a mean and SD of all values measured. * P < 0.05 for MN 800 Ag + k-CRG RV vs MN 800 Ag + k-CRG; **** P < 0.0001 for MN 800 Ag RV vs MN 800 Ag; ##### P < 0.0001 for MN 800 Ag + k-CRG RV vs MN 800 Ag RV; \$\$\$\$ P < 0.0001 for MN 800 Ag + k-CRG vs MN 800 Ag. £ represent P > 0.05, i.e., no statistical significance.

4.3.4. Permeation Assay

In an attempt to verify the ability of transdermal delivery of RV, aliquots obtained from the permeation assay were analyzed through HPLC. In this analysis, permeation medium was used to verify the influence of the compounds present in the skin in the basolateral samples.

A portion of a chromatogram regarding the identification of RV in the skin after 24 hours of contact with Exelon® patch is depicted in the figure below (Figure 24).

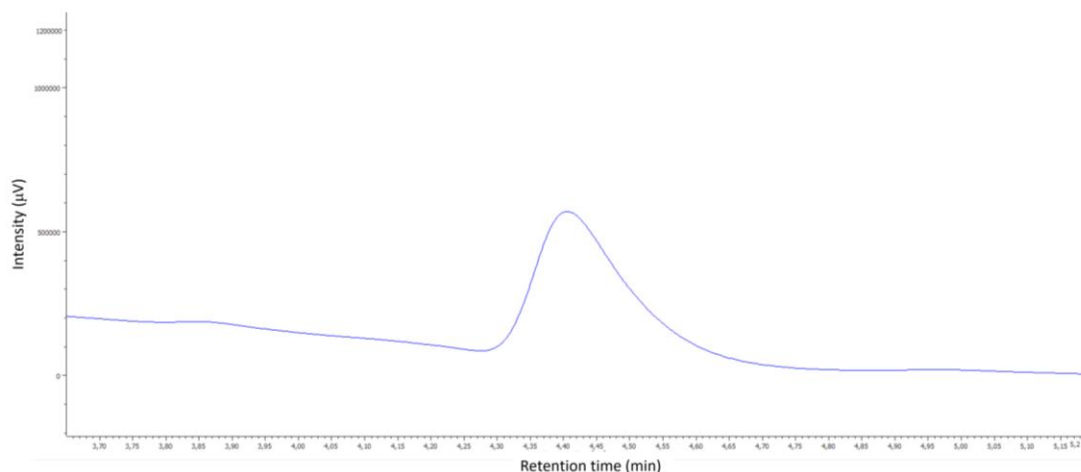


Figure 24 - Representative HPLC peak of a solution containing RV.

As controls for this study, Exelon® patch, and both hydrogel formulations were included. The hydrogels functioned as a measure for the influence of an MN system on drug delivery through the skin. Exelon patch® 5 cm², available in the market for transdermal delivery of RV, allowed to compare the drug in a form commercially available, but whose

drug bioavailability and irritability are not the most favorable. The measurements of drug release were performed cumulatively and are shown in Figure 25.

In all conditions, except for Exelon® patch, the percentage of permeation of RV increases over time reaching maximum values of approximately 100%. In the case of the marketed drug, as Exelon® patch needed to be cut for this study, the exact quantity of RV present in the portion of patch used is not exact, which can explain the permeation values closer to 200%. This event was observed in all three experiences, in which three different samples from a patch have been used. Since all 3 experiments verified the same phenomenon, the explanation may lie in the amount of drug found in each patch. That is, the area of 0.5 cm² that was cut from a 5 cm² patch was calculated to contain 0.9 mg of RV, assuming the drug was homogeneously distributed. However, given the percentages of permeation, the actual amount of RV present may be larger. One way to confirm this theory would be to destroy a patch portion and check the amount of RV present, which was not possible to perform during the time of the present work.

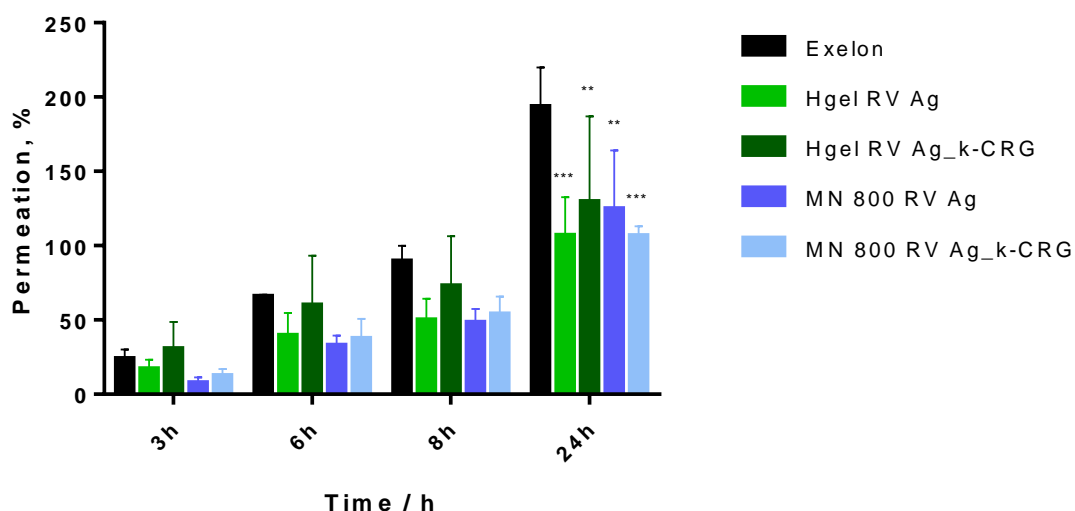


Figure 25 - RV permeation profile. Amount of permeated RV (%) as a function of time obtained for Exelon®, RV-loaded hydrogel, and RV-loaded MNs. **P < 0.01 for hydrogel formulation vs Exelon® at 24 hours; **P < 0.01 for MN 800 Alginate vs Exelon® at 24 hours; ***P < 0.001 for hydrogel formulations vs Exelon® at 24 hours; ***P < 0.001 for MN 800 Alginate + k-CRG vs Exelon® at 24 hours; The bars/points represent the mean ± SD of the permeability for three independent experiments (n=3).

For the remaining conditions, hydrogels and MNs, although all systems reached the 100% of permeation mark, it is however lower than that observed by the Exelon® patch. In view of a controlled-release system, these are more appropriate and can possibly be left for a period longer than the 24-hour study period described.

For all the timepoints, there was no significant difference in the delivery of RV through the skin (P > 0.05), between the MN systems and the RV-loaded hydrogels.

In this work were employed systems with 10% of the total drug mass (0.9 mg) used in the lowest dose transdermal patches, since Exelon® 5cm² has in total 9 mg of RV. Now, assuming the therapeutic dose to be 50% (4.6 mg per 24 hours) of the permeated RV, the therapeutic dose is obtained after 6h for all conditions.

Conclusions are in accordance with the data attained in the P_{app} calculations shown in Figure 26. No statistical significance is observed throughout the study, indicating that all delivery systems behave similarly.

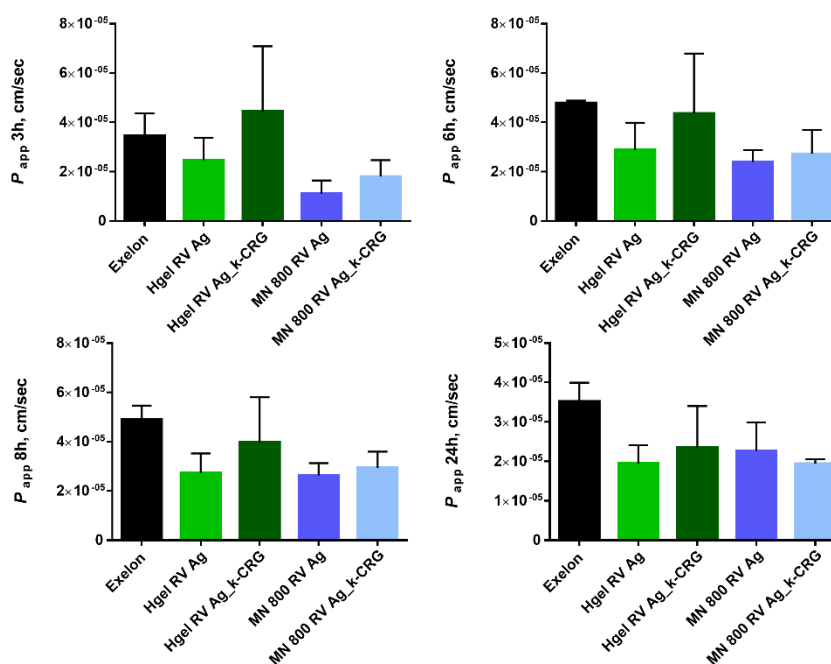


Figure 26 - Apparent permeability coefficient for 3, 6, 8, and 24 hours of RV for porcine ear skin treated with Exelon®, RV-loaded hydrogels, and RV-loaded MNs.

A study elaborated by Chauhan & Sharma, 2019 compares the delivery of RV between Exelon® patch (4.6 mg/24 hours) and optimized formulations of RV-loaded NLC integrating either eudragit E-100 or poly-butyl methacrylate-co-methyl methacrylate onto the patch. *In vitro* drug release study performed demonstrated that drug release was faster for Exelon® patch, with a percentage of 95.68% of release after 24 hours, while the nanocarriers patch matrix only reached the same percentage after 72 hours, beneficial for drug delivery systems looking for controlled release of the therapeutic formulation (Chauhan and Sharma 2019).

Another approach resorted to the delivery of RV using poly (lactic-co-glycolic acid) NPs for intranasal delivery embedded in a poloxamer 407® matrix. Drug release studies using the dialysis bag diffusion technique compared three different formulations of NPs with the respective RV-loaded hydrogel. Drug release was comprised, for NPs, between 43.28% and 60.41% while hydrogel formulation reached 62%. Although the gel formulation presented higher release, the profile of release of gel formulations containing NPs showed a more controlled release explained by the barrier RV must go through to be delivered. The results are in concordance with the results shown above (Bhatnagar *et al.* 2018).

After the permeation studies, both apical content and pig ear skin were collected, and drug quantification was performed by HPLC. Since the RV loaded in the donor compartment of the Franz cells permeated completely, according to Figure 25, it was expected that in the other components of the system the presence of this drug would only be residual. Figure 27 supports the conclusions reached. The majority of RV permeated the skin, while a small percentage remained in the apical or was retained in the pig skin.

These results confirm the potential of RV-loaded MNs to be a sustainable TDD system for a systemic release of the drug.

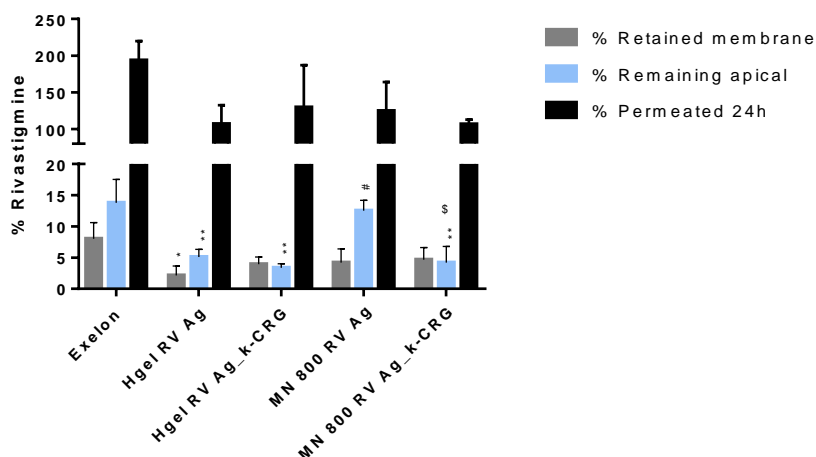


Figure 27 - Distribution of RV among permeated, retained, and non-permeated through the porcine skin after 24 hours. The bars/points represent the mean SD of the permeability for at least three independent experiments (n = 3). **P < 0.01 for Ag, Ag_k-CRG hydrogel formulation and MN 800 RV Ag_k-CRG vs Exelon® remaining in the apical; #P < 0.05 for MN 800 RV Ag vs hydrogel formulation remaining in the apical; \$ P < 0.05 for MN 800 RV Ag_k-CRG vs MN 800 RV Ag remaining in the apical; *P < 0.05 for Ag RV hydrogel formulation vs Exelon® retained in the membrane. Permeation statistical analysis can be seen in Figure 25.

The use of a transdermal patch requires contact of a patch with the skin for a certain period of time, which may trigger a negative response by the skin. Aspects such as the nature of the drug, the contact area, the existence of a history of allergy to any of the components, skin lesions, or duration of contact appear as risk factors for the development of skin reactions. A study conducted to evaluate skin tolerability to Exelon® patches of 10 cm² and 20 cm² reported that most of the skin reactions were considered “slight” or “mild” and consisted of pruritus and erythema, while more severe responses only concerned a small percentage of the patients under study (3-7%) (Cummings *et al.* 2010). Plus, Exelon® patch requires patch change every 24 hours with both material and RV expense, as only 50% is ultimately used by the patient.

Considering all this, the development of a MN system based on hydrogel is advantageous. Since hydrogels are associated with biocompatibility (Aravamudhan *et al.* 2014), in this particular case natural polymers, problems related to skin irritation can be circumvented. In addition, hydrogel-based MNs are an easy-to-use system, capable of enhancing drug-controlled release.

5. Conclusion and remarks

Throughout the work, three hydrogel formulations were successfully produced, alginate 7%, k-CRG 1%, and the mixture of both alginate + k-CRG (1:1) (w/w). A micromoulding technique was used to produce two types of MNs that differed in the height of the MN (400 or 800 μm). During the optimization process, it was noticeable that an equilibrium between the amount of drug added to the mould, the temperature, and rotation during the centrifugation process was essential for the success of the MN array.

Upon morphological analysis of all MN arrays produced using drug-free hydrogel, k-CRG 1% appeared to lack the characteristic 3D pyramidal structure of the MNs produced using the acquired moulds for both sizes. Given that, the formulation was removed from further testing.

MN systems made from alginate 7% and alginate + k-CRG (1:1) have been fully characterized using calcein as the model drug for this study. Observing the morphology of calcein-loaded MNs and, in comparison to MNs free of drug, the influence of calcein in the system can be verified. Calcein-loaded MNs appear not to suffer changes in structure. In both cases, it is possible to see deformations mainly in the first row of needles which can be explained by the detachment process used in this study. Moreover, in some cases, the base of the MN arrays presents rippling. This phenomenon may be due to the loss of water from the hydrogel matrix in an uncontrolled way. Additionally, when analyzing the height of the two types of MNs there was a discrepancy between the height promised by the mould and the actual height of the needles. Again, this phenomenon may be related to water loss in the hydrogel matrix or to the manufacturer's promised measurement, since the manufacturer may consider the height of the MN counting with the height of the base of the array. The presence of calcein did not affect the compression forces experienced by the alginate + k-CRG MNs. Contrarily, alginate MNs are responsive to the presence of calcein, in which the 400 μm height MNs experienced an increase in force, while the 800 μm MNs had a decrease in force. In general alginate MNs have a superior compression force all around.

Skin permeation study using calcein-loaded MNs showed permeation percentages close to 40%, in a more controlled release over 24 hours. This way the benefit for systemic delivery of alginate MNs, presenting a slower drug release is proven. The release profile allows the maintenance of the drug in plasma. Results have not shown a different release profile of the drug depending on the MN height, however considering the need for a device for systemic RV release, the 400 μm MNs were eliminated from further studies as they suggest a faster release profile and therefore more suitable for topical applications.

The skin-piercing ability of MNs was confirmed in all skin samples by fluorescence confocal and optical microscopy. On the one hand, the alteration of skin structures was verified by comparing all samples with controls: skin acquired a "lacy" appearance after contact with free calcein, which was also verified for calcein-loaded hydrogels in a smaller extension. These facts may explain the permeation values verified. Regarding the presence of perforations on the skin, these structures were visualized in all conditions containing MNs.

The application of the most promising MNs to the delivery of RV was assessed for alginate and alginate + k-CRG hydrogels with the 800 μm height micromould. As was visibly observed for the model drug, no changes in morphology were observed in RV-loaded MNs. Yet, alginate MNs showed a thinner structure compared to calcein. These changes are visible in some drug-free MNs and were not taken into consideration as it could be associated with the variability process within the MN production. Texture analysis demonstrated that the loading of RV provoked the increase in compression force of alginate MNs for values of 5.74 N and reduced by half the compression force of the mixture MNs to 0.45 N. In this instance, the influence of RV was visible for both hydrogels and shows that, in general, MNs produced with alginate have a higher compressive strength. Skin permeation studies with RV-loaded MNs showed that all conditions in the study reached 100% of permeation upon 24 hours of contact. In contrast to the herein-developed systems, Exelon® patch revealed a more rapid release of the drug over time. As early as 6 hours 50% of the total drug loaded for all systems permeated, which meant the therapeutic dosage was achieved for all conditions. The results from this assay validated the importance of an MN system for the controlled release of a drug, in this case, RV, through the skin barrier into the systemic circulation.

As a whole, the objective of this thesis was accomplished. The developed systems proved to be an asset in the delivery of the RV through the skin in a controlled manner. In this study, both 800 μm alginate and alginate + k-CRG MNs loaded with RV present themselves as competent systems for systemic delivery. Nevertheless, in the future, studies may be performed aiming to quantify the exact amount of RV in the portion of Exelon® patch, using the same method to determine the RV permeation profile (HPLC). Furthermore, it would be advantageous to develop more controlled and less time-consuming ways of producing these MNs. The introduction of a vacuum step to force the entry of the hydrogel into the cavities and avoid the mechanical wear of the centrifugation equipment can be an option. Moreover, it would be necessary to conduct studies on the tolerability of the developed approaches on the skin for a period of 24 hours or even longer periods, to prove the biocompatibility of the MNs and exploit their advantages over Exelon® patch.

6. References

- Abdo, Joseph, Nikolai Sopko, and Stephen Milner. 2020. "The Applied Anatomy of Human Skin: A Model for Regeneration." *Wound Medicine* 28:100179. doi: 10.1016/j.wndm.2020.100179.
- Alkilani, Ahlam Zaid, Maelíosa T. C. McCrudden, and Ryan F. Donnelly. 2015. "Transdermal Drug Delivery: Innovative Pharmaceutical Developments Based on Disruption of the Barrier Properties of the Stratum Corneum." *Pharmaceutics* 2015, Vol. 7, Pages 438-470 7:438-70. doi: 10.3390/PHARMACEUTICS7040438.
- Aoyagi, Seiji, Hayato Izumi, Yuichi Isono, Mitsuo Fukuda, and Hiroshi Ogawa. 2007. "Laser Fabrication of High Aspect Ratio Thin Holes on Biodegradable Polymer and Its Application to a Microneedle." *Sensors and Actuators A: Physical* 139:293-302. doi: 10.1016/J.SNA.2006.11.022.
- Aravamudhan, Aja, Daisy M. Ramos, Ahmed A. Nada, and Sangamesh G. Kumbar. 2014. "Natural Polymers: Polysaccharides and Their Derivatives for Biomedical Applications." Pp. 67-89 in *Natural and Synthetic Biomedical Polymers*. Elsevier. doi: 10.1016/B978-0-12-396983-5.00004-1
- Arshad, Muhammad Sohail, Sameen Fatima, Kazem Nazari, Radeyah Ali, Muhammad Farhan, Syed Aun Muhammad, Nasir Abbas, Amjad Hussain, Israfil Kucuk, Ming-Wei Chang, Prina Mehta, and Zeeshan Ahmad. 2020. "Engineering and Characterisation of BCG-Loaded Polymeric Microneedles." *Journal of Drug Targeting* 28:525-32. doi: 10.1080/1061186X.2019.1693577.
- Barbosa, Ana Isabel, Ana Joyce Coutinho, Sofia A. Costa Lima, and Salette Reis. 2019. "Marine Polysaccharides in Pharmaceutical Applications: Fucoidan and Chitosan as Key Players in the Drug Delivery Match Field." *Marine Drugs* 17:654. doi: 10.3390/MD17120654.
- Bhatnagar, Shubhmita, Amala Saju, Krishna Deepthi Cheerla, Sudeep Kumar Gade, Prashant Garg, and Venkata Vamsi Krishna Venuganti. 2018. "Corneal Delivery of Besifloxacin Using Rapidly Dissolving Polymeric Microneedles." *Drug Delivery and Translational Research* 8:473-83. doi: 10.1007/S13346-017-0470-8.
- Birks, Jacqueline S. 2006. "Cholinesterase Inhibitors for Alzheimer's Disease." in *Cochrane Database of Systematic Reviews*, edited by J. S. Birks. Chichester, UK: John Wiley & Sons, Ltd. doi: 10.1002/14651858.CD005593
- Brown, Thomas M., and Karthik Krishnamurthy. 2021. "Histology, Dermis." *StatPearls*. Retrieved September 10, 2021 (<https://www.ncbi.nlm.nih.gov/books/NBK535346/>).
- Cai, Yu, Qi Tian, Chao Liu, and Liang Fang. 2021. "Development of Long-Acting Rivastigmine Drug-in-Adhesive Patch Utilizing Ion-Pair Strategy and Characterization of Controlled Release Mechanism." *European Journal of Pharmaceutical Sciences* 161:105774. doi: 10.1016/j.ejps.2021.105774.
- Carrithers, Brennan, and Rif S. El-Mallakh. 2020. "Transdermal Asenapine in Schizophrenia: A Systematic Review." *Patient Preference and Adherence* 14:1541. doi: 10.2147/PPA.S235104.
- Chauhan, Meenakshi Kanwar, and Pankaj Kumar Sharma. 2019. "Optimization and Characterization of Rivastigmine Nanolipid Carrier Loaded Transdermal Patches for the Treatment of Dementia." *Chemistry and Physics of Lipids* 224:104794. doi: 10.1016/j.chemphyslip.2019.104794.
- Chen, Mei Chin, Ming Hung Ling, Kuan Ying Lai, and Esar Pramudityo. 2012. "Chitosan Microneedle Patches for Sustained Transdermal Delivery of Macromolecules." *Biomacromolecules* 13:4022-31. doi: 10.1021/bm301293d.
- Chen, Minglong, Guilan Quan, Ying Sun, Dan Yang, Xin Pan, and Chuanbin Wu. 2020. "Nanoparticles-Encapsulated Polymeric Microneedles for Transdermal Drug Delivery." *Journal of Controlled Release* 325:163-75. doi: 10.1016/j.jconrel.2020.06.039.
- Chen, Wei, Rui Tian, Can Xu, Bryant C. Yung, Guohao Wang, Yijing Liu, Qianqian Ni, Fuwu Zhang,

- Zijian Zhou, Jingjing Wang, Gang Niu, Ying Ma, Liwu Fu, and Xiaoyuan Chen. 2017. "Microneedle-Array Patches Loaded with Dual Mineralized Protein/Peptide Particles for Type 2 Diabetes Therapy." *Nature Communications* 2017 8:1 8:1-11. doi: 10.1038/s41467-017-01764-1.
- Cummings, Jeffrey L., Martin R. Farlow, Xiangyi Meng, Sibel Tekin, and Jason T. Olin. 2010. "Rivastigmine Transdermal Patch Skin Tolerability: Results of a 1-Year Clinical Trial in Patients with Mild-to-Moderate Alzheimers Disease." *Clinical Drug Investigation* 30:41-49. doi: 10.2165/11531270-000000000-00000.
- Dąbrowska, Agnieszka K., Christian Adlhart, Fabrizio Spano, Gelu-Marius Rotaru, Siegfried Derler, Lina Zhai, Nicholas D. Spencer, and René M. Rossi. 2016. "In Vivo Confirmation of Hydration-Induced Changes in Human-Skin Thickness, Roughness and Interaction with the Environment." *Biointerphases* 11:031015. doi: 10.1116/1.4962547.
- Dathathri, Eshwari, Satyapriya Lal, Mohit Mittal, Goutam Thakur, and Shounak De. 2019. "Fabrication of Low-Cost Composite Polymer-Based Micro Needle Patch for Transdermal Drug Delivery." *Applied Nanoscience* 2019 10:371-77. doi: 10.1007/S13204-019-01190-3.
- Datta, Deepanjan, Dhruvisha Sureshbhai Panchal, and Venkata Vamsi Krishna Venuganti. 2021. "Transdermal Delivery of Vancomycin Hydrochloride: Influence of Chemical and Physical Permeation Enhancers." *International Journal of Pharmaceutics* 602:120663. doi: 10.1016/j.ijpharm.2021.120663.
- Dening, Tom, and Malarvizhi Babu Sandilyan. 2015. "Dementia: Definitions and Types." *Nursing Standard (Royal College of Nursing (Great Britain): 1987)* 29:37-42. doi: 10.7748/ns.29.37.37.e9405.
- Dick, Ian P., and Robert C. Scott. 1992. "Pig Ear Skin as an In-vitro Model for Human Skin Permeability." *Journal of Pharmacy and Pharmacology* 44:640-45. doi: 10.1111/j.2042-7158.1992.tb05485.x.
- Dong, Yue, Zihao Wei, and Changhu Xue. 2021. "Recent Advances in Carrageenan-Based Delivery Systems for Bioactive Ingredients: A Review." *Trends in Food Science & Technology* 112:348-61. doi: 10.1016/J.TIFS.2021.04.012.
- Donnelly, Ryan F., Thakur Raghu Raj Singh, Ahlam Zaid Alkilani, Maelíosa T. C. McCrudden, Conor O'Mahony, Keith Armstrong, Nabla McLoone, Prashant Kole, and A. David Woolfson. 2013. "Hydrogel-Forming Microneedle Arrays Exhibit Antimicrobial Properties: Potential for Enhanced Patient Safety." *International Journal of Pharmaceutics* 451:76. doi: 10.1016/J.IJPHARM.2013.04.045.
- Donnelly, Ryan F., Thakur Raghu Raj Singh, and A. David Woolfson. 2010. "Microneedle-Based Drug Delivery Systems: Microfabrication, Drug Delivery, and Safety." *Drug Delivery* 17:187. doi: 10.3109/10717541003667798.
- Duong, Silvia, Tejal Patel, and Feng Chang. 2017. "Dementia: What Pharmacists Need to Know." *Canadian Pharmacists Journal* 150:118. doi: 10.1177/1715163517690745.
- Eldufani, Jabril, and Gilbert Blaise. 2019. "The Role of Acetylcholinesterase Inhibitors Such as Neostigmine and Rivastigmine on Chronic Pain and Cognitive Function in Aging: A Review of Recent Clinical Applications." *Alzheimer's & Dementia: Translational Research & Clinical Interventions* 5:175-83. doi: 10.1016/j.trci.2019.03.004.
- Fazil, Mohammad, Shadab Md, Shadabul Haque, Manish Kumar, Sanjula Baboota, Jasjeet Kaur Sahni, and Javed Ali. 2012. "Development and Evaluation of Rivastigmine Loaded Chitosan Nanoparticles for Brain Targeting." *European Journal of Pharmaceutical Sciences* 47:6-15. doi: 10.1016/j.ejps.2012.04.013.
- Ferreira-Vieira, Talita, Isabella Guimaraes, Flavia Silva, and Fabiola Ribeiro. 2016. "Alzheimer's Disease: Targeting the Cholinergic System." *Current Neuropharmacology* 14:101-15. doi: 10.2174/1570159x13666150716165726.
- Frew, Paula M., Michele Bennett Paine, Nadine Roupheal, Jay Schamel, Yunmi Chung, Mark J. Mulligan, and Mark R. Prausnitz. 2020. "Acceptability of an Inactivated Influenza Vaccine Delivered by Microneedle Patch: Results from a Phase I Clinical Trial of Safety, Reactogenicity, and Immunogenicity." *Vaccine* 38:7175-81. doi: 10.1016/J.VACCINE.2020.07.064.

- Gill, Harvinder S., and Mark R. Prausnitz. 2007. "Coated Microneedles for Transdermal Delivery." *Journal of Controlled Release: Official Journal of the Controlled Release Society* 117:227. doi: 10.1016/J.JCONREL.2006.10.017.
- González-Vázquez, Patricia, Eneko Larrañeta, Maelíosa T. C. McCrudden, Courtney Jarrachian, Annie Rein-Weston, Manjari Quintanar-Solares, Darin Zehring, Helen McCarthy, Aaron J. Courtenay, and Ryan F. Donnelly. 2017. "Transdermal Delivery of Gentamicin Using Dissolving Microneedle Arrays for Potential Treatment of Neonatal Sepsis." *Journal of Controlled Release* 265:30. doi: 10.1016/J.JCONREL.2017.07.032.
- Gothwal, Avinash, Kartik T. Nakhate, Amit Alexander, A. Ajazuddin, and Umesh Gupta. 2018. "Boosted Memory and Improved Brain Bioavailability of Rivastigmine: Targeting Effort to the Brain Using Covalently Tethered Lower Generation PAMAM Dendrimers with Lactoferrin." *Molecular Pharmaceutics* 15:4538-49. doi: 10.1021/acs.molpharmaceut.8b00537.
- Hanson, Leah R., and William H. Frey. 2008. "Intranasal Delivery Bypasses the Blood-Brain Barrier to Target Therapeutic Agents to the Central Nervous System and Treat Neurodegenerative Disease." *BMC Neuroscience* 9:S5. doi: 10.1186/1471-2202-9-s3-s5.
- Hardy, John, and David Allsop. 1991. "Amyloid Deposition as the Central Event in the Aetiology of Alzheimer's Disease." *Trends in Pharmacological Sciences* 12:383-88. doi: 10.1016/0165-6147(91)90609-V.
- Hong, Xiaoyun, Zaozhan Wu, Lizhu Chen, Fei Wu, Liangming Wei, and Weien Yuan. 2014. "Hydrogel Microneedle Arrays for Transdermal Drug Delivery." *Nano-Micro Letters* 2014 6:191-99. doi: 10.1007/BF03353783.
- Indermun, Sunaina, Regina Luttge, Yahya E. Choonara, Pradeep Kumar, Lisa C. Du Toit, Girish Modi, and Viness Pillay. 2014. "Current Advances in the Fabrication of Microneedles for Transdermal Delivery." *Journal of Controlled Release* 185:130-38. doi: 10.1016/J.JCONREL.2014.04.052.
- Ismail, Manal Fouad, Aliaa Nabil Elmeshad, and Neveen Abdel Hameed Salem. 2013. "Potential Therapeutic Effect of Nanobased Formulation of Rivastigmine on Rat Model of Alzheimer's Disease." *International Journal of Nanomedicine* 8:393-406. doi: 10.2147/IJN.S39232.
- Ita, Kevin. 2015. "Transdermal Delivery of Drugs with Microneedles—Potential and Challenges." *Pharmaceutics* 7:90. doi: 10.3390/PHARMACEUTICS7030090.
- Ita, Kevin. 2020. "Transcutaneous Drug Administration." Pp. 1-7 in *Transdermal Drug Delivery*. Elsevier. doi: 10.1016/b978-0-12-822550-9.00001-6
- Ito, Yukako, Junichi Ohta, Kazuki Imada, Shingo Akamatsu, Nozomi Tsuchida, Genta Inoue, Nana Inoue, and Kanji Takada. 2013. "Dissolving Microneedles to Obtain Rapid Local Anesthetic Effect of Lidocaine at Skin Tissue." *Journal of drug targeting* 21:770-75. doi: 10.3109/1061186X.2013.811510.
- Jann, Michael W. 2000. "Rivastigmine, a New-Generation Cholinesterase Inhibitor for the Treatment of Alzheimer's Disease." *Pharmacotherapy* 20:1-12. doi: 10.1592/phco.20.1.1.34664.
- Kalia, Lorraine V., and Anthony E. Lang. 2015. "Parkinson's Disease." *The Lancet* 386:896-912. doi: 10.1016/S0140-6736(14)61393-3.
- Kandiah, Nagaendran, Ming-Chyi Pai, Vorapun Senanarong, Irene Looi, Encarnita Ampil, Kyung Won Park, Ananda Krishna Karanam, and Stephen Christopher. 2017. "Rivastigmine: The Advantages of Dual Inhibition of Acetylcholinesterase and Butyrylcholinesterase and Its Role in Subcortical Vascular Dementia and Parkinson's Disease Dementia." *Clinical Interventions in Aging* 12:697. doi: 10.2147/CIA.S129145.
- Kim, Eun, Geza Erdos, Shaohua Huang, Thomas W. Kenniston, Stephen C. Balmert, Cara Donahue Carey, V. Stalin Raj, Michael W. Epperly, William B. Klimstra, Bart L. Haagmans, Emrullah Korkmaz, Louis D. Faló, and Andrea Gambotto. 2020. "Microneedle Array Delivered Recombinant Coronavirus Vaccines: Immunogenicity and Rapid Translational Development." *EBioMedicine* 55:102743. doi: 10.1016/J.EBIOM.2020.102743.
- Kim, Myoung Hwan, Yong Wook Lee, Won Kyo Jung, Junghwan Oh, and Seung Yun Nam. 2019. "Enhanced Rheological Behaviors of Alginate Hydrogels with Carrageenan for Extrusion-Based Bioprinting." *Journal of the Mechanical Behavior of Biomedical Materials* 98:187-94. doi: 10.1016/J.JMBBM.2019.06.014.

- Kitagawa, Reina, Hoathixuan Le, Paul Kiritsy, and Monica C. Chuong. 2020. "Formulation of Rivastigmine, a Liquid Drug Substance, for Use in a Simulating Study of Hollow Microstructured Transdermal Delivery System." *Journal of Pharmacology & Pharmaceutical Research* 3:1-6. doi: 10.31038/JPPR.2020333.
- Kurz, A., M. Farlow, and G. Lefèvre. 2009. "Pharmacokinetics of a Novel Transdermal Rivastigmine Patch for the Treatment of Alzheimer's Disease: A Review." *International Journal of Clinical Practice* 63:799. doi: 10.1111/J.1742-1241.2009.02052.X.
- Lee, Jeong Woo, Mee-Ree Han, and Jung-Hwan Park. 2013. "Polymer Microneedles for Transdermal Drug Delivery." *Journal of drug targeting* 21:211-23. doi: 10.3109/1061186X.2012.741136.
- Lee, Kwang, and Hyungil Jung. 2012. "Drawing Lithography for Microneedles: A Review of Fundamentals and Biomedical Applications." *Biomaterials* 33:7309-26. doi: 10.1016/J.BIOMATERIALS.2012.06.065.
- Legoabe, Lesetja J., Jaco C. Breytenbach, David D. N'Da, and J. Wilma Breytenbach. 2010. "In-Vitro Transdermal Penetration of Cytarabine and Its N4-Alkylamide Derivatives." *Journal of Pharmacy and Pharmacology* 62:756-61. doi: 10.1211/JPP.62.06.0012.
- Leone, M., J. Mönkäre, J. A. Bouwstra, and G. Kersten. 2017. "Dissolving Microneedle Patches for Dermal Vaccination." *Pharmaceutical Research* 34:2223-40. doi: 10.1007/S11095-017-2223-2.
- Li, Junwei, Mingtao Zeng, Hu Shan, and Chunyi Tong. 2017. "Microneedle Patches as Drug and Vaccine Delivery Platform." *Current Medicinal Chemistry* 24:2413-22. doi: 10.2174/0929867324666170526124053.
- Madson, Kimberly A., and Sherrill Brown. 2016. "Rivastigmine: Dementia with Lewy Bodies." *Hospital Pharmacy* 51:129-31. doi: 10.1310/hpj5102-129.
- Makvandi, Pooyan, Melissa Kirkby, Aaron R. J. Hutton, Majid Shabani, Cynthia K. Y. Yiu, Zahra Baghbantaraghdari, Rezvan Jamaledin, Marco Carlotti, Barbara Mazzolai, Virgilio Mattoli, and Ryan F. Donnelly. 2021. "Engineering Microneedle Patches for Improved Penetration: Analysis, Skin Models and Factors Affecting Needle Insertion." *Nano-Micro Letters* 2021 13:1-41. doi: 10.1007/S40820-021-00611-9.
- Maldonado Loyo, Héctor, and Luis Niño De Rivera Y Oyarzabal. 2011. "Mixed Wet and Dry Etching Techniques for Microneedles Fabrication." *CCE 2011 - 2011 8th International Conference on Electrical Engineering, Computing Science and Automatic Control, Program and Abstract Book*. doi: 10.1109/ICEEE.2011.6106701.
- Marwah, Harneet, Tarun Garg, Amit K. Goyal, and Goutam Rath. 2016. "Permeation Enhancer Strategies in Transdermal Drug Delivery." *Drug Delivery* 23:564-78. doi: 10.3109/10717544.2014.935532.
- Menon, Gopinathan K., Gary W. Cleary, and Majella E. Lane. 2012. "The Structure and Function of the Stratum Corneum." *International Journal of Pharmaceutics* 435:3-9. doi: 10.1016/j.ijpharm.2012.06.005.
- Moniz, Tânia, Sofia A. Costa Lima, and Salette Reis. 2020a. "Application of the Human Stratum Corneum Lipid-Based Mimetic Model in Assessment of Drug-Loaded Nanoparticles for Skin Administration." *International Journal of Pharmaceutics* 591. doi: 10.1016/J.IJPHARM.2020.119960.
- Moniz, Tânia, Sofia A. Costa Lima, and Salette Reis. 2020b. "Human Skin Models: From Healthy to Disease-Mimetic Systems; Characteristics and Applications." *British Journal of Pharmacology* 177:4314-29. doi: 10.1111/bph.15184.
- Moniz, Tânia, Sofia A. Costa Lima, and Salette Reis. 2021. "Marine Polymeric Microneedles for Transdermal Drug Delivery." *Carbohydrate Polymers* 266:118098. doi: 10.1016/j.carbpol.2021.118098.
- Moosavi, Seyed Mojtaba, and Sussan Ghassabian. 2018. "Linearity of Calibration Curves for Analytical Methods: A Review of Criteria for Assessment of Method Reliability." in *Calibration and Validation of Analytical Methods - A Sampling of Current Approaches*. InTech. doi: 10.5772/intechopen.72932
- Musumeci, Teresa, Rosalia Pellitteri, Michela Spatuzza, and Giovanni Puglisi. 2014. "Nose-to-Brain

- Delivery: Evaluation of Polymeric Nanoparticles on Olfactory Ensheathing Cells Uptake.” *Journal of Pharmaceutical Sciences* 103:628-35. doi: 10.1002/JPS.23836.
- Nagarkar, Rigved, Mahima Singh, Hiep X. Nguyen, and Sriramakamal Jonnalagadda. 2020. “A Review of Recent Advances in Microneedle Technology for Transdermal Drug Delivery.” *Journal of Drug Delivery Science and Technology* 59:101923. doi: 10.1016/J.JDDST.2020.101923.
- Ng, Keng Wooi, and Wing Man Lau. 2015. “Skin Deep: The Basics of Human Skin Structure and Drug Penetration.” Pp. 3-11 in *Percutaneous Penetration Enhancers Chemical Methods in Penetration Enhancement*. Berlin, Heidelberg: Springer Berlin Heidelberg. doi: 10.1007/978-3-662-45013-0_1
- Oh, Jae Ho, Hyoung Hyang Park, Ki Young Do, Manhee Han, Dong Hun Hyun, Chang Gyu Kim, Chang Hyeon Kim, Seung S. Lee, Sung Joo Hwang, Sang Chul Shin, and Cheong Weon Cho. 2008. “Influence of the Delivery Systems Using a Microneedle Array on the Permeation of a Hydrophilic Molecule, Calcein.” *European Journal of Pharmaceutics and Biopharmaceutics* 69:1040-45. doi: 10.1016/J.EJPB.2008.02.009.
- Panza, Francesco, Madia Lozupone, Giancarlo Logroscino, and Bruno P. Imbimbo. 2019. “A Critical Appraisal of Amyloid-B-Targeting Therapies for Alzheimer Disease.” *Nature Reviews Neurology* 15:73-88. doi: 10.1038/s41582-018-0116-6.
- Panza, Francesco, Madia Lozupone, Davide Seripa, and Bruno P. Imbimbo. 2019. “Amyloid-B Immunotherapy for Alzheimer Disease: Is It Now a Long Shot?” *Annals of Neurology* 85:303-15. doi: 10.1002/ana.25410.
- Park, Jung Hwan, Seong O. Choi, Rachna Kamath, Yong Kyu Yoon, Mark G. Allen, and Mark R. Prausnitz. 2007. “Polymer Particle-Based Micromolding to Fabricate Novel Microstructures.” *Biomedical Microdevices* 9:223-34. doi: 10.1007/S10544-006-9024-4.
- Pattarabhiran, Srijanaki Paravastu, Anjana Saju, Kanchan Rajendra Sonawane, Raghuraman Manimaran, Shubhmita Bhatnagar, Girdhari Roy, Radha Balkrishna Kulkarni, and Venkata Vamsi Krishna Venuganti. 2019. “Dissolvable Microneedle-Mediated Transcutaneous Delivery of Tetanus Toxoid Elicits Effective Immune Response.” *AAPS PharmSciTech* 20:257. doi: 10.1208/S12249-019-1471-3.
- Pérennès, F., B. Marmioli, M. Matteucci, M. Tormen, L. Vaccari, and E. Di Fabrizio. 2006. “Sharp Beveled Tip Hollow Microneedle Arrays Fabricated by LIGA and 3D Soft Lithography with Polyvinyl Alcohol.” *Journal of Micromechanics and Microengineering* 16:473-79. doi: 10.1088/0960-1317/16/3/001.
- Prausnitz, Mark R., and Robert Langer. 2008. “Transdermal Drug Delivery.” *Nature Biotechnology* 26:1261-68. doi: 10.1038/nbt.1504.
- Proksch, Ehrhardt, Johanna M. Brandner, and Jens-Michael Jensen. 2008. “The Skin: An Indispensable Barrier.” *Experimental Dermatology* 17:1063-72. doi: 10.1111/j.1600-0625.2008.00786.x.
- Qureshi, Dilshad, Suraj Kumar Nayak, Samarendra Maji, Doman Kim, Indranil Banerjee, and Kunal Pal. 2019. “Carrageenan: A Wonder Polymer from Marine Algae for Potential Drug Delivery Applications.” *Current Pharmaceutical Design* 25:1172-86. doi: 10.2174/1381612825666190425190754.
- Ramadon, Delly, Maeliosa T. C. McCrudden, Aaron J. Courtenay, and Ryan F. Donnelly. 2021. “Enhancement Strategies for Transdermal Drug Delivery Systems: Current Trends and Applications.” *Drug Delivery and Translational Research* 1-34. doi: 10.1007/s13346-021-00909-6.
- Ravic, G., N. Vishal Gupta, and V. Balamuralidhara. 2018. “Rivastigmine Tartrate Solid Lipid Nanoparticles Loaded Transdermal Film: An in Vivo Study.” *Research Journal of Pharmacy and Technology* 11:227-30. doi: 10.5958/0974-360X.2018.00042.2.
- Del Rio-Sancho, S., C. E. Serna-Jiménez, M. A. Calatayud-Pascual, C. Balaguer-Fernández, A. Femenía-Font, V. Merino, and A. López-Castellano. 2012. “Transdermal Absorption of Memantine - Effect of Chemical Enhancers, Iontophoresis, and Role of Enhancer Lipophilicity.” *European Journal of Pharmaceutics and Biopharmaceutics* 82:164-70. doi: 10.1016/j.ejpb.2012.06.005.

- Roxhed, Niclas, Björn Samel, Lina Nordquist, Patrick Griss, and Göran Stemme. 2008. "Painless Drug Delivery through Microneedle-Based Transdermal Patches Featuring Active Infusion." *IEEE Transactions on Biomedical Engineering* 55:1063-71. doi: 10.1109/TBME.2007.906492.
- Sabri, Akmal H., Yujin Kim, Maria Marlow, David J. Scurr, Joel Segal, Ajay K. Banga, Leonid Kagan, and Jong Bong Lee. 2020. "Intradermal and Transdermal Drug Delivery Using Microneedles - Fabrication, Performance Evaluation and Application to Lymphatic Delivery." *Advanced Drug Delivery Reviews* 153:195-215. doi: 10.1016/J.ADDR.2019.10.004.
- Sadeghi, Mohsen, Fariba Ganji, Seyyed Mojtaba Taghizadeh, and Bahram Daraei. 2016. "Preparation and Characterization of Rivastigmine Transdermal Patch Based on Chitosan Microparticles." *Iranian Journal of Pharmaceutical Research* 15:283-94. doi: 10.22037/IJPR.2016.1889.
- Sadowsky, C., J. A. Davil. Perez, R. W. Bouchard, I. Goodman, and S. Tekin. 2010. "Switching from Oral Cholinesterase Inhibitors to the Rivastigmine Transdermal Patch." *CNS Neuroscience and Therapeutics* 16:51-60. doi: 10.1111/j.1755-5949.2009.00119.x.
- Sadowsky, Carl H., Joseph L. Micca, George T. Grossberg, and Drew M. Velting. 2014. "Rivastigmine from Capsules to Patch: Therapeutic Advances in the Management of Alzheimer's Disease and Parkinson's Disease Dementia." *Primary Care Companion to the Journal of Clinical Psychiatry* 16. doi: 10.4088/PCC.14r01654.
- Shah, Brijesh, Dignesh Khunt, Himanshu Bhatt, Manju Misra, and Harish Padh. 2015. "Application of Quality by Design Approach for Intranasal Delivery of Rivastigmine Loaded Solid Lipid Nanoparticles: Effect on Formulation and Characterization Parameters." *European Journal of Pharmaceutical Sciences* 78:54-66. doi: 10.1016/j.ejps.2015.07.002
- Shakel, Zinaida, Cláudia Nunes, Sofia A. Costa Lima, and Salette Reis. 2019. "Development of a Novel Human Stratum Corneum Model, as a Tool in the Optimization of Drug Formulations." *International Journal of Pharmaceutics* 569:118571. doi: 10.1016/J.IJPHARM.2019.118571.
- Shravanth, S. H., Riyaz Ali M. Osmani, Jyothi S. L, V. P. Anupama, Mohamed Rahamathulla, and H. V. Gangadharappa. 2021. "Microneedles-Based Drug Delivery for the Treatment of Psoriasis." *Journal of Drug Delivery Science and Technology* 64:102668. doi: 10.1016/J.JDDST.2021.102668.
- Singh, Parbeen, Andrew Carrier, Yongli Chen, Sujing Lin, Jinlin Wang, Shufen Cui, and Xu Zhang. 2019. "Polymeric Microneedles for Controlled Transdermal Drug Delivery." *Journal of Controlled Release* 315:97-113. doi: 10.1016/J.JCONREL.2019.10.022.
- Small, Gary, and Bruno Dubois. 2007. "A Review of Compliance to Treatment in Alzheimer's Disease: Potential Benefits of a Transdermal Patch." *Current Medical Research and Opinion* 23:2705-13. doi: 10.1185/030079907X233403.
- Subramony Anand, J. 2013. "Needle Free Parenteral Drug Delivery: Leveraging Active Transdermal Technologies for Pediatric Use." *International Journal of Pharmaceutics* 455:14-18. doi: 10.1016/J.IJPHARM.2013.07.055.
- Tønnesen, Hanne Hjorth, and Jan Karlsen. 2002. "Alginate in Drug Delivery Systems." *Drug Development and Industrial Pharmacy* 28:621-30. doi: 10.1081/DDC-120003853.
- Triarhou, Lazaros C. 2013. "Dopamine and Parkinson's Disease." *Madame Curie Bioscience Database*. Retrieved June 23, 2021 (<https://www.ncbi.nlm.nih.gov/books/NBK6271/>).
- Vintiloiu, Anda, Michel Lafleur, Guillaume Bastiat, and Jean-Christophe Leroux. 2007. "In Situ-Forming Oleogel Implant for Rivastigmine Delivery." *Pharmaceutical Research* 25:845-52. doi: 10.1007/S11095-007-9384-3.
- Waghule, Tejashree, Gautam Singhvi, Sunil Kumar Dubey, Murali Monohar Pandey, Gaurav Gupta, Mahaveer Singh, and Kamal Dua. 2019. "Microneedles: A Smart Approach and Increasing Potential for Transdermal Drug Delivery System." *Biomedicine & Pharmacotherapy* 109:1249-58. doi: 10.1016/J.BIOPHA.2018.10.078.
- Wang, Qi Lei, Jia Wei Ren, Bo Zhi Chen, Xuan Jin, Can Yang Zhang, and Xin Dong Guo. 2018. "Effect of Humidity on Mechanical Properties of Dissolving Microneedles for Transdermal Drug Delivery." *Journal of Industrial and Engineering Chemistry* 59:251-58. doi: 10.1016/J.JIEC.2017.10.030.

- Xenikakis, Iakovos, Manolis Tzintzimis, Konstantinos Tsongas, Dimitrios Andreadis, Euterpi Demiri, Dimitrios Tzetzis, and Dimitrios G. Fatouros. 2019. "Fabrication and Finite Element Analysis of Stereolithographic 3D Printed Microneedles for Transdermal Delivery of Model Dyes across Human Skin in Vitro." *European Journal of Pharmaceutical Sciences* 137:104976. doi: 10.1016/J.EJPS.2019.104976.
- Xie, Song, Zijing Li, and Zongqin Yu. 2015. "Microneedles for Transdermal Delivery of Insulin." *Journal of Drug Delivery Science and Technology* 28:11-17. doi: 10.1016/J.JDDST.2015.04.008.
- Yao, Donggang. 2009. "Micromolding of Polymers." *Advances in Polymer Processing* 552-78. doi: 10.1533/9781845696429.4.552.
- Yousef, Hani, and Sandeep Sharma. 2018. "Anatomy, Skin (Integument), Epidermis." *StatPearls*. Retrieved July 3, 2021 (<http://www.ncbi.nlm.nih.gov/pubmed/29262154>).
- Yu, Weijiang, Guohua Jiang, Yang Zhang, Depeng Liu, Bin Xu, and Junyi Zhou. 2017. "Polymer Microneedles Fabricated from Alginate and Hyaluronate for Transdermal Delivery of Insulin." *Materials Science and Engineering C* 80:187-96. doi: 10.1016/J.MSEC.2017.05.143.
- Yu, Zhen Wei, Yi Liang, and Wen Quan Liang. 2015. "Low-Frequency Sonophoresis Enhances Rivastigmine Permeation in Vitro and in Vivo." *Pharmazie* 70:379-80. doi: 10.1691/PH.2015.4191.
- Zaric, Marija, Pablo Daniel Becker, Catherine Hervouet, Petya Kalcheva, Barbara Ibarzo Yus, Clement Cocita, Lauren Alexandra O'Neill, Sung Yun Kwon, and Linda Sylvia Klavinskis. 2017. "Long-Lived Tissue Resident HIV-1 Specific Memory CD8+ T Cells Are Generated by Skin Immunization with Live Virus Vected Microneedle Arrays." *Journal of Controlled Release* 268:166-75. doi: 10.1016/J.JCONREL.2017.10.026.
- Zhong, Hao, Ging Chan, Yuanjia Hu, Hao Hu, and Defang Ouyang. 2018. "A Comprehensive Map of FDA-Approved Pharmaceutical Products." *Pharmaceutics* 10. doi: 10.3390/PHARMACEUTICS10040263.